Available online at www.sciencedirect.com
SCIENCE DIRECT®
Journal of Colloid and Interface Science 276 (2004) 420–438
JOURNAL OF Colloid and Interface Science
www.elsevier.com/locate/jcis

Foam drainage on the microscale I. Modeling flow through single Plateau borders

S.A. Koehler [a,*], S. Hilgenfeldt [b], H.A. Stone [c]

[a] *Physics Department, Emory University, Atlanta, GA 303022, USA*
[b] *Faculty of Applied Physics, University of Twente, PO Box 217, 7500 AE Enschede, The Netherlands*
[c] *Division of Engineering and Applied Sciences, Harvard University, Cambridge, MA 02138, USA*

Received 14 July 2003; accepted 20 December 2003

Available online 15 June 2004

Abstract

The drainage of liquid through a foam involves flow in channels, also called Plateau borders, which generally are long and slender. We model this flow by assuming the flow is unidirectional, the shear is transverse to the flow direction, and the liquid/gas interfaces are mobile and characterized by a Newtonian surface viscosity, which does not depend on the shear rate. Numerical finite difference simulations are performed, and analytical approximations for the velocity fields inside the channels and the films that separate the bubbles are given. We compare the liquid flow rates through interior channels, exterior channels (i.e., channels contacting container walls) and films. We find that when the number of exterior channels is comparable to the number of interior channels, i.e., narrow container geometries, the exterior channels can significantly affect the dynamics of the drainage process. Even for highly mobile interfaces, the films do not significantly contribute to the drainage process, unless the amount of liquid in the films is within a factor of ten of the amount of liquid in the channels.

Keywords: Foams; Emulsions; Surface rheology

1. Introduction

Foams have numerous applications in the food, construction and chemical industries, and their properties frequently are of interest to chemists, engineers, mathematicians and physicists [1–5]. To better understand fundamental mechanisms that influence the processing steps of foamed materials, as well as to potentially suggest new uses of foams, requires a more complete description of the flow behavior at both the microscopic and macroscopic scales; not surprisingly, the latter depends on the former. Such investigations naturally offer insight into fundamental questions concerning the flow, rheology, and response of other complex liquids (e.g., emulsions, colloids, suspensions, surfactant solutions, etc.). One aspect of the dynamics of foams concerns drainage, which refers to the motion of liquid relative to the bubbles that make up the foam. Here we extend previous work [6,7] focusing on the influence of surface shear viscosity by presenting both numerical and analytical models for the manner in which surface shear viscosity impacts drainage rates in the long slender channels, or Plateau borders, that form the interconnected fluid network of a foam. In a similar spirit, we model the flow through the thin films that separate the bubbles. While several simplifications are necessary to obtain a tractable model, we seek to understand foam drainage on the microscale by providing a detailed description of the effects of interfacial mobility and film thickness. As experiments on the micro-scale become more sophisticated, the assumptions made in these models can be checked and refined. We refer to the studies at the scale of a single channel as *microscopic*, which is to be contrasted with *macroscopic* descriptions at the scale of at least several bubbles.

In recent years, there have been many studies of the foam drainage process. A wide variety of questions have been asked including characterizing different types of drainage configurations (forced, free and pulsed drainage) [8–10], flows in two-dimensional geometries [11,12], the influence

* Corresponding author.
E-mail address: skoehler@physics.emory.edu (S.A. Koehler).
URL: http://www.physics.emory.edu/faculty/koehler.

0021-9797/$ – see front matter
doi:10.1016/j.jcis.2003.12.061

of container shape [13], the influence of bubble size on drainage [14,15], the impact of different surfactants on the drainage process [16,17] and the influence of suspended polymers in the foam solution [18]. The thickness variations of the films that separate bubbles have been investigated [15], possibly suggesting that these films may play an important role in foam drainage [19,20]. In several cases, quantitative comparisons have been made between the results of macroscopic experiments and corresponding macroscopic, mean-field, drainage models. Often the agreement is reasonable, but quantitative discrepancies, both within the results from a given laboratory as well as between different laboratories performing similar experiments, have encouraged attempts for more rational modeling by more closely examining the microscopic assumptions that form the basis of the macroscopic models. The flow behavior of the liquid/gas interface of the bubbles in a foam appears to play a prominent role and hence we present a theoretical study (Part 1) and experimental investigations (Part 2) at the scale of a single Plateau border with the aim of providing more insight into one aspect of the potential role of interfacial rheology.

Although it has been known for several decades that surfactants affect many properties of foams, only recently has there been research that strongly suggests that *microscopic* mechanisms may influence *macroscopic* drainage rates in foams. Most experiments have been performed with low liquid volume fractions where most of the liquid exists in the narrow Plateau borders which are connected, via nodes, to form a network through which fluid flows owing to gravity and capillary action. Thus, the idea of channel-dominated [21] as contrasted with node-dominated [14] drainage was suggested as a way to explain different types of observed foam drainage behavior. Durand et al. [16] showed that both limits were accessible in the same experimental configuration by changing the amount of dodecanol in an SDS surfactant solution, which is known to strongly influence the interfacial rheology. Furthermore they showed that macroscopic drainage rates were influenced in a manner consistent with the channel-dominated versus node-dominated paradigm. To further investigate the dependence of the interfacial rheology on the macroscopic drainage rates, Koehler et al. [17] used confocal microscopy to directly measure the velocity profiles in individual Plateau borders. The velocity profiles found for foams stabilized by small molecule surfactants differed from foams stabilized by high molecular weight surfactants. These studies of the rheological impact of the surfactants used to make the foam are consistent with studies showing the influence of surfactants on the interfacial mobility of isolated soap films suspended on wire frames [22].

An important step in the microscopic modeling of the rheological impact of the surfactant in a foam was made by Leonard and Lemlich [6,23], who developed a microscopic model for uniaxial flow through channels based upon velocity gradients transverse to the flow direction and surface viscosity. Later Desai and Kumar developed analytical approximations for the microscopic model introduced by Leonard and Lemlich and compared this model with measurements of the average velocity of liquid draining through a foam [24]. Recently Nguyen improved on the numerical calculations of Leonard and Lemlich and numerically determined correlations between the surface viscosity and the flow velocity [7]. In this work, we extend the basic microscopic model in several ways: (i) we consider flow through exterior channels (at the container wall), (ii) we consider flows through films, (iii) we find scaling behavior for the flows, (iv) we provide analytical formulas for the flow rates, and (v) we compare the flow rates through exterior channels and films with that of interior channels. This treatment of foam drainage on the micro scale should prove useful for understanding and further developing more realistic models of foam drainage on both the microscopic and the macroscopic scales.

2. Geometry of interior and exterior channels and films

Foams are composed of gas and a small volume of liquid that separates the bubbles. A useful geometric idealization is to consider the foam composed of identical tetrakaidecahedral bubbles as shown in Fig. 1a, along with its surrounding channels and nodes. We shall consider foams with low liquid volume fractions $\epsilon \lesssim 0.05$, where the channels are long and slender. We denote the channel length by L, which also sets the scale of the lateral dimensions of the films. In this paper, we will focus on the fluid dynamics of two simpler elements of the continuous phase, which are the films and the channels, and do not consider the nodes, which are the intersections of four channels and have flow that is far from unidirectional.

Foams are often inside of containers, and therefore it is necessary to distinguish between *interior* and *exterior* channels as distinct pathways for drainage. Interior channels are the interstitial regions between three touching bubbles as shown in Fig. 1b, whereas exterior bubbles are the regions between two touching bubbles and a container wall, as shown in Fig. 1c. The container wall is treated as flat. For small foam containers, the relative number of exterior and interior channels is significant, and macroscopic drainage experiments have been performed indicating that container size can affect foam drainage [25].

We are interested in calculating the flow through channels and providing estimates of flows through films, which in turn depend on the cross-sectional areas of these different geometric elements. The natural length scale for channels is the transverse radius of curvature, or more precisely the radius of curvature of the section across the channel's middle, which we shall denote by a. As shown in Fig. 2, the edges of the channels are connected to the edges of the films, of half-thickness w, and when the films are thin, the dominant contribution to the channel's cross-sectional area comes

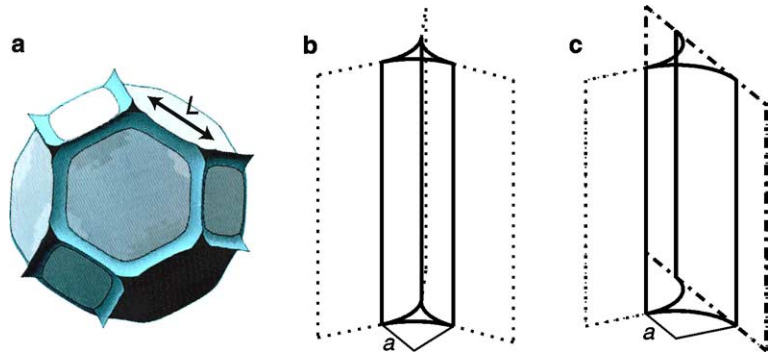

Fig. 1. (a) Drawing of a tetrakaidecahedral cell, an idealized bubble in a foam with liquid volume fraction $\epsilon = 0.005$ (courtesy of A. Kraynik). The bubble has 14 films, 12 nodes and 36 channels that have length L. (b) Sketch of an interior channel (solid lines), which is the interstitial space between three neighboring bubbles and has radius of curvature a. The dotted lines indicate the three films separating the three bubbles. (c) Sketch of an exterior channel, which is the interstitial space between two neighboring bubbles and the container wall. The dotted line indicates the film, and the dashed line with dots indicates the container wall.

from a. We assume that the film thickness does not vary much, due to capillary forces within the film that tend to uniformly distribute liquid and remove curvature on the films. The half-width of the film is denoted by H ($w \ll H$), which depends on the number of sides of the film and the channel length L. For example a hexagonal film has a full-width of about $2H \approx 2\sqrt{3}L$, depending on the orientation for a regular hexagonal face, whereas for a square face $2H \approx L$. For the purposes of providing upper bounds on the flow through thin films the approximation $H \approx L$ is adequate.

The symmetry units of the three geometric elements under consideration are indicated by the shaded regions of Fig. 2. The cross-sectional areas of the symmetry units for the films, interior channels and exterior channels are

$$A_{\text{film}}(w; H) = wH, \tag{1a}$$

$$A_{\text{int}}(w; a) = \left(\sqrt{3}(a+w)^2 - \pi a^2/2\right)/6, \tag{1b}$$

$$A_{\text{ext}}(w; a) = (a+w)^2 - \pi a^2/4. \tag{1c}$$

For negligible film thicknesses, $w \ll a$, the total cross-sectional area of the exterior channel is $\approx 0.43a^2$, and the total cross-sectional area of the interior channel is $\approx 0.16a^2$, which is a noteworthy difference for small containers where the number of exterior channels is significant. As we show later in Section 5.2, the flow rate through an exterior channel can be as large as seven times the flow rate of an interior channel of equivalent width a.

The geometry of the elements varies with the liquid volume fraction, and if the contribution of the films is included, the liquid volume fraction of an idealized Kelvin foam can be approximated by [26]

$$\epsilon \approx 0.171\left(\frac{a}{L}\right)^2 + 0.20\left(\frac{a}{L}\right)^3 + 2.4\left(\frac{w}{L}\right). \tag{2}$$

The second term is the contribution of the nodes to the liquid volume, and often has been neglected [27], which is valid provided $a \ll L$. The last term is the contribution from the films, and has generally also been neglected, which is valid provided that $w \ll 10^{-1}a^2/L$ [15].

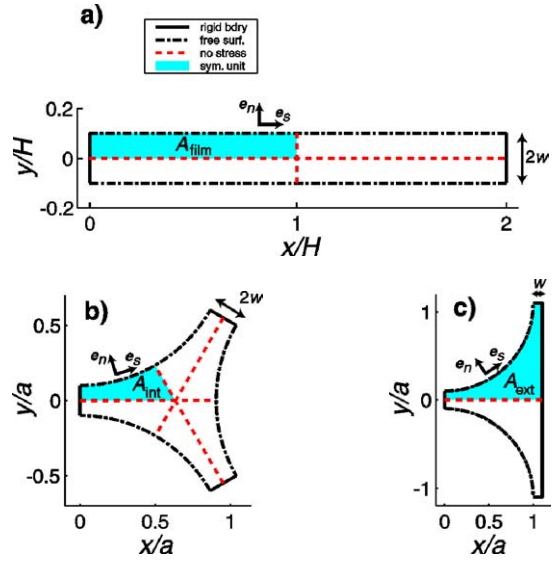

Fig. 2. The cross-section of (a) a film, where the film half thickness is $w = 0.1H$ (*not* drawn to scale), (b) an interior channel and (c) an exterior channel, where $w = 0.1a$. The shaded regions are symmetry units, which have dimensional areas A_{film}, A_{int} and A_{ext} for the films, interior, and exterior channels respectively. The dashed lines show the symmetry of the velocity fields where the shear stresses are zero, the solid lines show the rigid boundaries, and the dashed lines with dots show the free surfaces. The arrows indicate the direction of the unit normal $\mathbf{e}_n$ which is directed outward, and the tangent $\mathbf{e}_s$ at the liquid/gas interface.

3. Governing equations

In order to describe flow in channels, we make use of the assumptions originally proposed by Leonard and Lemlich [6], which are in agreement with experimental observations of velocity profiles across single channels [17]. At low liquid volume fractions, $\epsilon \lesssim 0.05$, the channels are long and slender, so neglecting axial variations is expected to be a very good assumption. Furthermore we limit the description of the velocity distribution to a purely axial flow so the liquid velocity depends only on the position within the channel's cross section. Second, we assume that the interfacial rheology is entirely determined by a Newtonian surface viscosity,

and neglect other effects such as Marangoni forces due to variations in the surfactant concentration at the interfaces. Third, we assume that the velocity is close to zero where the channel merges into the film [28]. Finally, we assume that the flow is viscously dominated so that Stokes equations can be used. We align the z-axis with the direction of the flow, and denote the angle to the vertical by θ, with $0 \leqslant \theta \leqslant \pi/2$. Because the flow is essentially unidirectional through the channels, the axial (scalar) velocity u inside the Plateau border is related to the driving force, G, by

$$\mu \nabla^2 u + G = 0 \quad \text{where } G = -\partial p/\partial z + \rho g \cos\theta, \tag{3}$$

where p is the liquid pressure, μ is the bulk viscosity and ρg is the gravitational force per unit volume. The choice for the direction of the z axis is axially along the direction of flow, with the z axis pointing downward at an angle of θ to the vertical. Since the cross-sectional area does not vary significantly in the flow direction, capillary forces, which depend on the curvature of the liquid/gas interface, are negligible and we can assume that the driving force for the flow is also not changing significantly with z.

In Fig. 2 the cross-sections of a film, interior and exterior channels are drawn using a dimensionless Cartesian coordinate system. We defer the treatment of the films to Appendix A, and focus on the interior and exterior channels drawn in Figs. 2b and 2c. The shaded regions of Figs. 2b and 2c (also reproduced in Figs. 5 and 9) are the symmetry units of the interior and exterior channels, with the origin placed at the corner to the left. The velocity fields are symmetric about the dashed lines, so the shearing stresses along the dashed lines are zero. The characteristic length scale is a, and the characteristic velocity scale is $U_{\text{channel}} \equiv a^2 G/\mu$. Quantities rescaled by the channel's radius of curvature carry the superscript $\tilde{}$, for example the film's dimensionless half-thickness is $\tilde{w} = w/a$. Thus we need to solve Poisson's equation, $\tilde{\nabla}^2 \tilde{u} = -1$, which requires numerical treatment owing to the unusual geometries; however we present analytical approximations in Section 4.

To describe the boundary conditions on the velocity fields we define the normal and tangent vectors, $\mathbf{e}_n$ and $\mathbf{e}_s$ respectively, to a surface given by $y = h(x)$ (see Fig. 2),

$$\mathbf{e}_n = \frac{1}{\sqrt{1+h'^2}}(\mathbf{e}_y - h'\mathbf{e}_x) \quad \text{and}$$
$$\mathbf{e}_s = \frac{1}{\sqrt{1+h'^2}}(\mathbf{e}_x + h'\mathbf{e}_y), \tag{4}$$

where primes denote differentiation with respect to x.

For the symmetry unit of the interior channel, see Fig. 2b, the bottom boundary is at $\tilde{y} = 0$, and the top boundary, which consists of a left and a right region, is at

$$\tilde{y} = h_{\text{int}}(\tilde{x}; \tilde{w}) \quad \text{where}$$
$$h_{\text{int}}(\tilde{x}; \tilde{w}) = \begin{cases} (1+\tilde{w}) - \sqrt{1-\tilde{x}^2} & \text{for } 0 \leqslant \tilde{x} \leqslant 1/2, \\ (1+\tilde{w}) - \sqrt{3}\tilde{x} & \\ \quad \text{for } 1/2 \leqslant \tilde{x} \leqslant (1+\tilde{w})/\sqrt{3}. \end{cases} \tag{5}$$

The boundary conditions on the flow for the interior channel are [29]

$$\frac{\partial \tilde{u}}{\partial \tilde{y}} = 0 \quad \text{at } \tilde{y} = 0, \text{ for } 0 \leqslant \tilde{x} \leqslant (1+\tilde{w})/\sqrt{3}, \tag{6a}$$
$$\frac{\partial \tilde{u}}{\partial n} = 0 \quad \text{at } \tilde{y} = 1 + \tilde{w} - \sqrt{3}\tilde{x}, \tag{6b}$$
$$\tilde{u} = 0 \quad \text{at } \tilde{x} = 0, \text{ for } 0 \leqslant \tilde{y} \leqslant \tilde{w}, \tag{6c}$$
$$\left(\frac{\partial}{\partial s}\right)^2 \tilde{u}_s = M \frac{\partial \tilde{u}}{\partial n} \quad \text{at } \tilde{y} = h_{\text{int}}(\tilde{x}; \tilde{w}), \text{ for } 0 \leqslant \tilde{x} \leqslant 1/2,$$

where

$$M \equiv \frac{\mu a}{\mu_s}. \tag{6d}$$

The surface velocity is explicitly denoted as $\tilde{u}_s(\tilde{x}) \equiv \tilde{u}(\tilde{x}, h_{\text{int}}(\tilde{x}; \tilde{w}))$. The first two conditions indicate symmetry of the flow across the boundaries on the bottom and right side, respectively. The third boundary condition is the assumption that the velocity is zero at the edge of the Plateau border, where the film is connected, and will be discussed in more detail below. The last condition (6c) is the coupling between surface and bulk layer, which is set by the interfacial mobility M [30].

For the exterior channel, Fig. 2c, the boundaries are similar to those of the interior channel, and the top boundary is

$$\tilde{y} = h_{\text{ext}}(\tilde{x}; \tilde{w}) \quad \text{where}$$
$$h_{\text{ext}}(\tilde{x}; \tilde{w}) = \begin{cases} (1+\tilde{w}) - \sqrt{1-\tilde{x}^2} & \text{for } 0 \leqslant \tilde{x} < 1, \\ (1+\tilde{w}) & \text{for } 1 \leqslant \tilde{x} \leqslant 1+\tilde{w}. \end{cases} \tag{7}$$

Also the Neumann (zero stress) boundary condition at the right that is used for interior channels has been changed to a Dirichlet (zero velocity) boundary condition

$$\tilde{u} = 0 \quad \text{at } \tilde{x} = 1 + \tilde{w}, \tag{8}$$

and the boundary at the top supports no stress,

$$\frac{\partial \tilde{u}}{\partial \tilde{y}} = 0 \quad \text{at } \tilde{y} = 1 + \tilde{w}. \tag{9}$$

Aside from the driving force, G, the dynamics for both interior and exterior channels depend on the four parameters with dimensions μ_s, μ, w, a, which can be combined into two dimensionless parameters M and $\tilde{w}$. We show below that these two dimensionless parameters can further be combined into a single composite parameter, Λ, that describes the dynamics.

A description of the flow in the films is far more complicated. Unlike results for channels [17] which show that the flow is essentially unidirectional, experiments have shown that for films there is substantial circulation. The flow along the edges of films is typically upwards, which is *opposite* to the flow in the channels and the middle of the films where the direction of the flow is downward. These motions are likely due to Marangoni forces which generally produce surface pressure gradients that oppose the flow.

For obtaining estimates we apply the same treatment used for channels for a simplified model of unidirectional flow through films neglecting Marangoni forces in Appendix A. Including Marangoni forces for a more realistic scenario should lead to an opposing secondary flow. Thus the simplified model for films should prove useful for setting upper bounds on the flow through films, which in turn sets upper bounds on the possible contribution of films to the macroscopic drainage process.

4. Analytical and numerical results

The original numerical computation of the flow field inside a Plateau border with the realistic shape shown in Fig. 2b was performed by Leonard and Lemlich [6], who used a finite-difference approach and fully implemented all of the boundary conditions (6). Most importantly, the authors recognized the potential importance of interfacial rheology, which they incorporated by accounting for the shear viscosity of the surfactant layer. Nguyen recently reported similar numerical work using improved numerical resolution and also presented several correlations that fit the numerical results [7]. In Appendix B we present a convenient procedure applicable for thin surface films for converting the top-most boundary condition at the interface with the gas phase, $y = h(x)$, into a Neumann (zero stress) boundary condition, while retaining the effect of interfacial shear in the surfaces of the Plateau borders. This approach allows for successful simulations of the flow using standard software packages, such as MATLAB. Fig. 3 shows calculations of the velocity fields of interior and exterior channels using this procedure. In the following, the numerical results are compared with asymptotic descriptions of the flow field that aid in developing physical intuition for the ways in which surface mobility impacts the bulk flow.

Before going into details a few general remarks should be useful. From the standpoint of a mean field theory for macroscopic foam drainage, the quantity of interest is the average liquid velocity in the channels, which depends on the interfacial mobility, M, and the film thickness, $\tilde{w}$. Shown in Fig. 4 is the dependence of the average dimensionless velocity of interior and exterior channels on the interfacial mobility for a variety of film thicknesses. The velocity fields monotonically increase with increasing interfacial mobility. However for interior channels increasing the film thickness can either increase or decrease the average velocity depending on the interfacial mobility. In this section we develop analytical arguments to describe the dependence of the velocity on M and $\tilde{w}$. In particular we find that for both types of channels there is a dimensionless parameter $\Lambda = \mu a/(\mu_s + \mu w) = M/(1 + M\tilde{w})$, which allows for rescaling of the average velocities for all the simulations onto master curves (see Fig. 12 in Section 4.3). We discuss the physical meaning of this parameter and present analytical arguments for the velocity profiles.

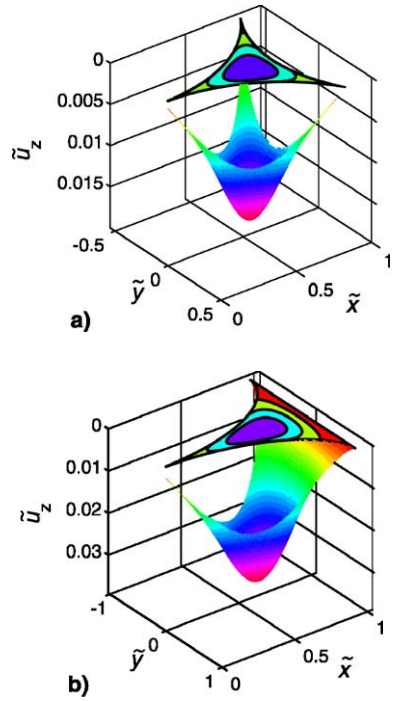

Fig. 3. Numerically computed velocity fields for (a) an interior channel and (b) an exterior channel, for the case of semi-mobile interfaces, $M = 1$ and film thickness $\tilde{w} = 0$. For semi-mobile interfaces, the liquid velocity at the liquid/gas interface is comparable to the maximum velocity at the center of the Plateau border. Three evenly spaced contour lines are shown in the $(\tilde{x}, \tilde{y})$-plane.

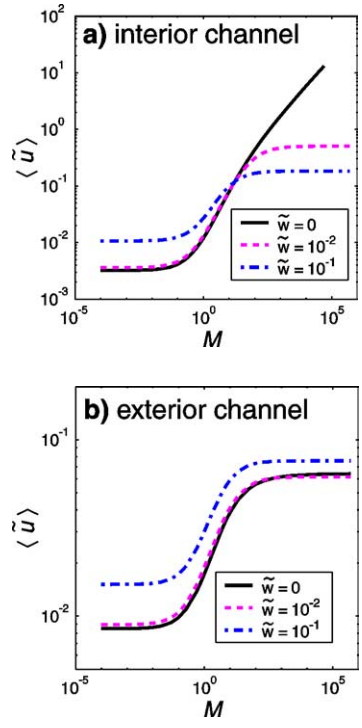

Fig. 4. The dependence of the average velocity on the interfacial mobility for (a) interior channels and (b) exterior channels with different edge thicknesses as indicated in the legends.

4.1. An integral method for establishing the variations in surface velocity

Although the detailed velocity fields of the Plateau borders require numerical calculation, certain quantitative and qualitative features of the flow can be established using an elementary physical argument. This argument is based upon a force balance for a control area, which involves the gravitational force that drives the flow, and is opposed by shear stresses along the periphery of the control area that arise from both the rigid boundaries and the surfactant-laden interfaces. The flow in channels is unidirectional, and we apply the force balance to interior and exterior channels. An analogous treatment for the idealized thin film problem is given in Appendix A, which provides an estimate of the upper bound for the volumetric flow through the films due to gravitationally driven drainage.

4.1.1. Asymptotic estimates for interior channels

Consider a control area for the cross section of an interior channel with a certain film thickness. Two examples are shown by the shaded regions of Fig. 5. Since the Reynolds number is small, the gravitational force on the fluid is balanced by shear stresses (both from the bulk and the surface film) which act at the periphery of the control area. There are non-zero shear stresses only at the left edge of the control region, because of the symmetry condition on the flow at the bottom and right sides, and at the curved interface the shearing of the fluid against the gas inside the bubble is negligible. Thus the "weight," which is the area of shaded region, $\tilde{A}_{\rm supp}(\tilde{x};\tilde{w})$, is supported by the shearing stress along the left edge.

The area of the fluid inside the control area, extending from some value of $\tilde{x}$ to the edge on the right, $\tilde{x} = (1+\tilde{w})/\sqrt{3}$, is

$$\tilde{A}_{\rm supp}(\tilde{x};\tilde{w}) \equiv \int_{\tilde{x}}^{(1+\tilde{w})/\sqrt{3}} h_{\rm int}(x';\tilde{w})\,dx'. \tag{10}$$

The two-dimensional "weight" of this control area is entirely supported by shearing at $\tilde{x}$, which is the left side of the control region, and leads to the force balance

$$\tilde{A}_{\rm supp}(\tilde{x};\tilde{w}) = \int_{y'=0}^{h_{\rm int}(\tilde{x};\tilde{w})} (\mathbf{e}_x\cdot\nabla)\tilde{u}(\tilde{x},y')\,dy' + M^{-1}(\mathbf{e}_x\cdot\nabla)\tilde{u}_s(\tilde{x}) = 0, \tag{11}$$

where $-\mathbf{e}_x$ is the unit normal at the left-hand boundary of the control surface pointing out of the control area, as indicated by the arrow in Fig. 5b. The first term on the right-hand side is the opposing force from shearing the bulk liquid at $\tilde{x}$, and the second term arises from shearing at the free surface, $(\tilde{x}, h_{\rm int}(\tilde{x};\tilde{w}))$.

The velocity field of the channel can be represented as the sum of the surface velocity, $\tilde{u}_s$, and an internal velocity component, $\tilde{u}_1$,

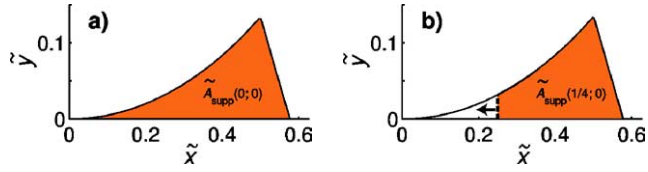

Fig. 5. Schematic diagrams of the control region for calculating the force balance on an interior channel, where the film thickness is zero. The shaded region is $\tilde{A}_{\rm supp}$, whose "weight" is supported by shearing at (a) the left edge, $\tilde{x} = 0$ (and so $\tilde{A}_{\rm supp} = \tilde{A}_{\rm int}$), and (b) at the dashed line, $\tilde{x} = 1/4$. The arrow in (b) shows the orientation of the shearing plane at the left-hand boundary of the control area.

$$\tilde{u}(\tilde{x},\tilde{y}) = \tilde{u}_s(\tilde{x}) + \tilde{u}_1(\tilde{x},\tilde{y}), \tag{12}$$

where $\tilde{u}_1(\tilde{x}, h_{\rm int}(\tilde{x};\tilde{w})) = 0$. For a completely rigid interface, $M = 0$, the surface velocity is zero and $\tilde{u}_1$ is the fluid velocity that solves (3).

A simple expression for the surface velocity is obtained by replacing $\tilde{u}$ in (11) with (12),

$$\frac{d\tilde{u}}{d\tilde{x}} = \left(\tilde{A}_{\rm supp}(\tilde{x};\tilde{w}) - \int_{y'=0}^{h_{\rm int}(\tilde{x};\tilde{w})} \frac{\partial\tilde{u}_1(\tilde{x},y')}{\partial\tilde{x}}\,dy'\right) \Big/ \left(h_{\rm int}(\tilde{x};\tilde{w}) + M^{-1}\right). \tag{13}$$

The height of the channels is small, $h_{\rm int}(\tilde{x};\tilde{w}) \ll 1$, because the films are thin, and so the dominant variations of the internal velocity component are along $\tilde{y}$, making a lubrication-theory approach useful (see Section 4.2). The internal velocity component increases with increasing $\tilde{x}$, and neglecting it in (13) leads to an approximate equation for the variations of the surface velocity that depends on M and the shape of the Plateau border:

$$\frac{d\tilde{u}}{d\tilde{x}} \lesssim \frac{M\tilde{A}_{\rm supp}(\tilde{x};\tilde{w})}{1+Mh_{\rm int}(\tilde{x};\tilde{w})}. \tag{14}$$

For small values of $\tilde{x}$, a good approximation for the shape variation is the parabolic profile $h_{\rm int}(\tilde{x};\tilde{w}) \approx \tilde{w} + \tilde{x}^2/2$, and $\tilde{A}_{\rm supp}(\tilde{x};\tilde{w}) \approx \tilde{A}_{\rm int}(\tilde{w})$ [31].

Then Eq. (14) simplifies to

$$\frac{d\tilde{u}_s}{d\tilde{x}} \lesssim \frac{\Lambda\tilde{A}_{\rm int}(\tilde{w})}{(1+\Lambda\tilde{x}^2/2)} - \tilde{w}\Lambda x + \mathcal{O}(\tilde{x})^3 \quad \text{where} \quad \Lambda \equiv \frac{M}{1+M\tilde{w}}. \tag{15}$$

The dimensionless composite parameter can also be written as $\Lambda = \mu a/(\mu_s + \mu w)$, showing that this is a ratio of the product of the bulk viscosity and the characteristic size of the channel to the combined surface viscosity and product of the bulk viscosity and the edge thickness. A large value of Λ corresponds to both small edge thickness and low surface viscosity, so the velocity increases rapidly from the edge, because the shear stresses in the thin bulk region have to support the "weight" $\tilde{A}_{\rm int}(\tilde{w})$ (cf. Eq. (14)). A small value of

Λ corresponds to either a large surface viscosity or relatively thick face, which in turn leads to a slower increase in the velocity with increasing distance from the edge. Integrating the leading term from Eq. (15) with $\tilde{u}_s(0) = 0$ yields (here we have not included the inequality)

$$\frac{\tilde{u}_s(\tilde{x})}{\tilde{A}_{\text{int}}(\tilde{w})} \approx (2\Lambda)^{1/2} \arctan(\tilde{x}\sqrt{\Lambda/2}). \tag{16}$$

This result illustrates that the scale of variation of the dimensionless velocity as well as the maximum dimensionless surface velocity is set by the weight of the cross-sectional area, $\tilde{A}_{\text{int}}(\tilde{w})$, and the single parameter Λ.

Fig. 6a shows the numerically computed surface velocities $\tilde{u}_s(\tilde{x})$ as a function of position in the channel, rescaled using the result from Eq. (16) as a guide, and compared directly with the prediction of (16). The agreement between the approximate formula and the numerical results is very good, with the approximation being somewhat larger for three reasons: (i) the contribution of the internal velocity component in (13) was dropped, (ii) the higher-order terms from (14) have been dropped, and (iii) the area of the channel is overestimated by setting $\tilde{A}_{\text{supp}}(\tilde{x};\tilde{w}) = \tilde{A}_{\text{int}}(\tilde{w})$ in (16).

By symmetry considerations, the maximum surface velocity is located at the upper right-hand corner of the symmetry unit drawn in Fig. 5, at $(1/2, \tilde{w}+1-\sqrt{3/4})$. Together with (16) the maximum surface velocity varies with Λ and $\tilde{w}$ as

$$\max(\tilde{u}_s) \approx (2\Lambda)^{1/2} \tilde{A}_{\text{int}}(\tilde{w}) \arctan(\sqrt{\Lambda/8}). \tag{17}$$

For the case $\tilde{w} = 0$ and large interfacial mobilities and with (1b) the maximum surface velocity is $\max(\tilde{u}_s) \approx (\sqrt{3} - \pi/2)(\pi/6)(M/2)^{1/2} \approx 0.060 M^{1/2}$. We point out that this is compatible with the numerical results for the *average* velocity found by Nguyen [7] in the limit of large interfacial mobilities [32].

We now explore the behavior of the internal velocity component by focusing on the centerline velocity $\tilde{u}_1(\tilde{x}, 0)$, which should be small because the symmetry unit is narrow. For points on the centerline further from the rigid boundary, and closer to the free surface, $h(\tilde{x};\tilde{w}) \lesssim \tilde{x}$, we expect that velocity gradients along the y-axis dominate, which is the lubrication-theory approach. Fig. 6b shows the internal velocity component along the centerline normalized by the channel height, $\tilde{u}_1(\tilde{x}, 0)/h(\tilde{x};\tilde{w})^2$, plotted against $\tilde{x}/\tilde{w}$ for a range of different film thicknesses and interfacial mobilities. It can be seen that $\tilde{u}_1(\tilde{x}, 0) \sim h(\tilde{x};\tilde{w})^2$ for points $\tilde{w} \lesssim \tilde{x}$; however the scaling predicted by lubrication theory only holds roughly due to the complicated geometry of the channel. For points close to the rigid boundary, $\tilde{x} \lesssim \tilde{w}$, the centerline velocity scales linearly with position: $\tilde{u}_1(\tilde{x}, 0) \sim \tilde{x}/\tilde{w}$. Close to the rigid boundary, the geometry resembles that of a thin film, and the internal velocity component of thin films has similar scaling behavior (see Appendix A).

In Fig. 7a the rescaled maximum surface velocity, $\max(\tilde{u}_s)$, and the average channel velocity, $\langle\tilde{u}\rangle$, are plotted against Λ for two film thicknesses $\tilde{w} = 0$ and $\tilde{w} = 0.1$. In the limit of large M, the maximum surface velocity, maximum bulk velocity and average velocity approach each other, since the velocity variations in the y-direction are small compared with the velocity variations in the x-direction. The maximum surface velocities collapse onto the analytical approximation (17). The average channel velocity, $\langle\tilde{u}\rangle$, also collapses; however it only agrees with the surface approximation (17) for $\Lambda \gtrsim 1$, where both the interfaces are mobile, $M > 1$, and the films are thin, $\tilde{w} \ll 1$.

Variations of the channel edge width, $\tilde{w}$, also have important qualitative and quantitative effects on the flow that are coupled to the interfacial mobility M. Fig. 7b shows the average velocity rescaled by the channel area, $\langle\tilde{u}\rangle/\tilde{A}_{\text{int}}(\tilde{w})$, as a function of $\tilde{w}$ for different interfacial mobilities. For larger mobilities, $M \gg 1$, increasing the film thickness $\tilde{w}$ leads to a *decrease* in the channel velocity, because the length of the rigid boundary increases. For small mobilities, $M \ll 1$, the ratio $\langle\tilde{u}\rangle/\tilde{A}_{\text{int}}(\tilde{w})$ is essentially independent of $\tilde{w}$, because the boundaries are basically rigid, which makes the flow Poiseuille-like, and the flow roughly scales with the cross-sectional area.

It is also informative to examine the relative amounts of energy dissipated per unit height of the channel at the interface and in the bulk. The dimensionless bulk dissipation and

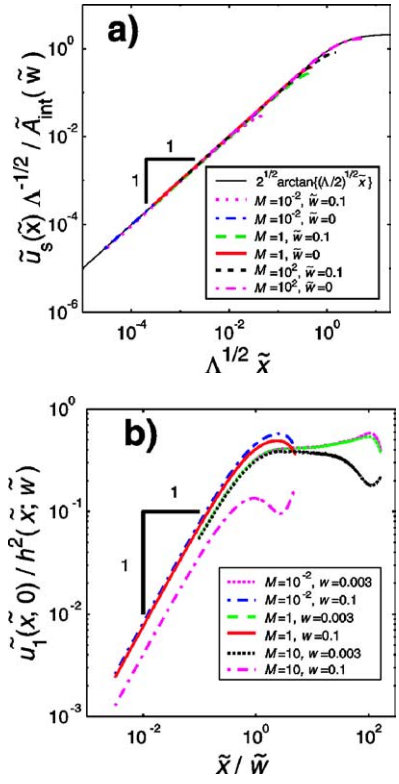

Fig. 6. (a) Simulations for interior channels of the rescaled surface velocity, $\tilde{u}_s(\tilde{x})$. The asymptotic solution (16) is indicated by the solid thin line. (b) The internal velocity component rescaled by the channel height is plotted against the position along the centerline rescaled by the film thickness.

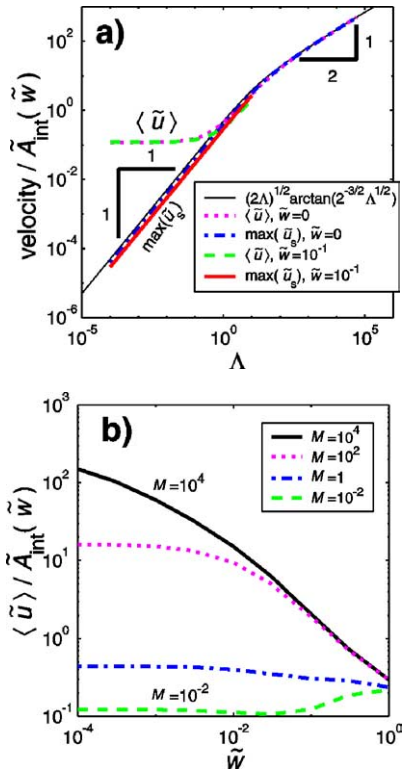

Fig. 7. (a) Simulations for the rescaled velocities plotted against Λ. The asymptotic solution (17) agrees well with the simulations for the maximum surface velocity, $\max(\tilde{u}_s)$. The average channel velocity, $\langle \tilde{u} \rangle$, also collapses well using this scaling. (b) The effect of the channel edge width, $\tilde{w}$, on the average channel velocity for different interfacial mobilities, $M = 10^{-2}, 1, 10^2, 10^4$.

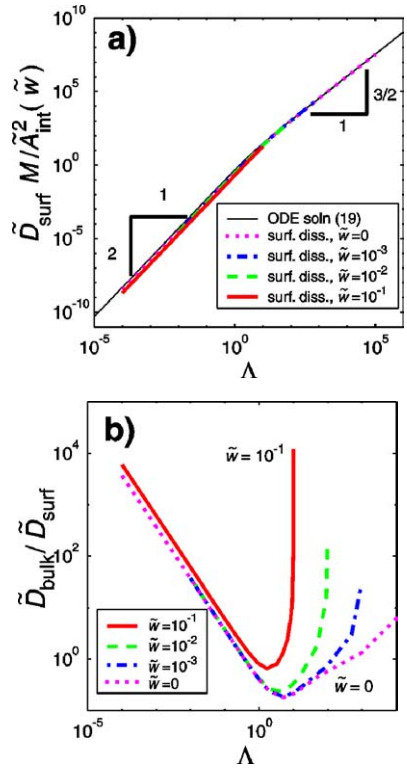

Fig. 8. (a) Simulations of the rescaled power dissipated in the surface plotted against the rescaled interfacial mobility for the film thicknesses $\tilde{w} = 0, 10^{-3}, 10^{-2}, 10^{-1}$. The results are superimposed on the estimate (19) which is indicated by the thin solid line. (b) The dependence of ratio of the power dissipated in the bulk to the power dissipated in the surface is plotted against Λ.

surface dissipation are, respectively,

$$\tilde{\mathcal{D}}_{\text{bulk}} = \int \left\{ \left(\frac{\partial \tilde{u}}{\partial \tilde{x}} \right)^2 + \left(\frac{\partial \tilde{u}}{\partial \tilde{y}} \right)^2 \right\} d\tilde{x}\, d\tilde{y}, \tag{18a}$$

$$\tilde{\mathcal{D}}_{\text{surf}} = M^{-1} \int \left(\frac{\partial \tilde{u}_s}{\partial \tilde{s}} \right)^2 d\tilde{s}. \tag{18b}$$

Fig. 8a shows that the surface dissipation results collapse onto a universal curve as a function of Λ for different film thicknesses. The thin solid curve in the figure shows the estimated dissipation calculated using (16), where velocity variations along the y-direction are neglected, and is

$$\tilde{\mathcal{D}}_{\text{surf}} \approx \left\{ \frac{2\Lambda^2}{8+\Lambda} + \frac{\Lambda^{3/2}}{\sqrt{2}} \operatorname{arccot}\left(\sqrt{\frac{8}{\Lambda}} \right) \right\} \frac{\tilde{A}_{\text{int}}(\tilde{w})^2}{M}. \tag{19}$$

Agreement with the numerical results [33] is good. Fig. 8b shows that for most values of Λ the dissipation in the bulk dominates. Only for a certain range of values of $\Lambda \gtrsim 1$ and $\tilde{w} \lesssim 10^{-2}$ does the surface dissipation become significant [34], which is experimentally realized for certain soap foams (see Part 2).

4.1.2. Asymptotic estimates for exterior channels

For exterior channels, a similar integral approach with some modifications can be taken as for interior channels. The key difference between the interior and exterior channels is that the exterior channel has *two* rigid boundaries, at $\tilde{x} = 0$ and $\tilde{x} = 1 + \tilde{w}$, as compared with only one for the interior channel; compare Figs. 2b and 2c. We consider the "weight" of a control area that is entirely supported by shearing at the left edge of the control area. This control area extends to the right and ends where the shear stress in the x-direction is zero. The zero-stress line depends on the velocity field, which in turn depends on M and $\tilde{w}$, so we need three parameters to describe the area supported by shearing at $\tilde{x}$, which has "weight" $\tilde{A}_{\text{supp}}(0; M, \tilde{w})$.

We proceed by locating the position $\tilde{x}_{\max}$ of the maximum of the centerline velocity, which is where the shear stress is zero (i.e., $(\partial \tilde{u}/\partial \tilde{x})(\tilde{x}_{\max}, 0) = 0$). Because the channels are slender, the component of the shear stress normal to the line $\tilde{x} = \tilde{x}_{\max}$ should be close to zero. The "weight" of the supported region approximately is

$$\tilde{A}_{\text{supp}}(\tilde{x}; M, \tilde{w}) \approx \int_{\tilde{x}}^{\tilde{x}_{\max}} h_{\text{ext}}(x'; \tilde{w})\, dx', \tag{20}$$

and in Fig. 9 three examples of estimates for the region supported at $\tilde{x} = 0$ are shown with different choices of film thicknesses and interfacial mobilities. Unlike interior chan-

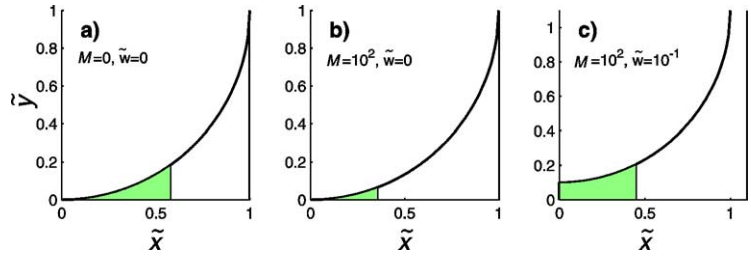

Fig. 9. Estimates of $\tilde{A}_{\rm supp}(0; M; \tilde{w})$, the "weight" of the control region supported by shearing at the left corner, $\tilde{x} = 0$, shown as shaded. This weight is used for calculating the force balance (20) and depends on M and $\tilde{w}$. The shaded region in (a) is for $\tilde{w} = 0$ and rigid interfaces, (b) is for $\tilde{w} = 0$, $M = 10^2$, and (c) is for $\tilde{w} = 0.1$, $M = 10^2$. Note that the "weight" of the unshaded region on the right is supported by shearing at container wall, $\tilde{x} = 1 + \tilde{w}$.

nels, the supported "weight" also depends on M in addition to $\tilde{w}$ (compare Fig. 5 with Fig. 9).

We can apply arguments similar to those for the interior channel (see Eqs. (13) and (16)), to estimate the interfacial velocity,

$$\frac{d\tilde{u}_s}{d\tilde{x}} \approx \frac{\Lambda \tilde{A}_{\rm supp}(\tilde{x}; M, \tilde{w})}{1 + \Lambda \tilde{x}^2/2} \quad \text{for } \tilde{x} \leqslant \tilde{x}_{\max}. \tag{21}$$

This can be integrated to obtain a result nearly identical to (16):

$$\frac{\tilde{u}_s}{\tilde{A}_{\rm supp}(\tilde{x}; M, \tilde{w})} \approx (2\Lambda)^{1/2} \arctan\left(\tilde{x}\sqrt{\Lambda/2}\right) \quad \text{for } \tilde{x} \leqslant \tilde{x}_{\max}. \tag{22}$$

Rescaling the surface velocity by $\tilde{A}_{\rm supp}(0; M, \tilde{w})\Lambda^{1/2}$ and the position by $\Lambda^{1/2}$ collapses the numerical data for a large range of parameters; results are shown in Fig. 10a. The thin solid curve for the approximation (22) agrees well with the collapsed data. Using the same approximations as with interior channels, the weight of the region supported by shearing at $\tilde{x} \leqslant \tilde{x}_{\max}$ can be approximated by $\tilde{A}_{\rm supp}(0; M, \tilde{w})$, and in the limit of large Λ the right-hand side of (22) approaches $\pi(\Lambda/2)^{1/2}$. This gives an asymptotic result for the maximum surface velocity similar to (17):

$$\max(\tilde{u}_s) \approx \pi\sqrt{\Lambda/2}\,\tilde{A}_{\rm supp}(0; M, \tilde{w}). \tag{23}$$

For different film thicknesses the supported area and the position of the maximum centerline velocity also depend on Λ as shown in Fig. 10b for three different values of the film thicknesses. The estimated area supported by the left edge, $\tilde{A}_{\rm supp}(0; M, \tilde{w})$, is scaled by the total area of the symmetry unit (see (1c)), and collapses for different film thicknesses when plotted against Λ. We thus identify the area of the supported channel by the left edge as a function of $(\Lambda, \tilde{w})$ and provide an ad-hoc estimate,

$$\frac{\tilde{A}_{\rm supp}(0; M, \tilde{w})}{\tilde{A}_{\rm ext}(\tilde{w})} \approx g(\Lambda) \quad \text{where}$$
$$g(\Lambda) = 0.3\left\{\arctan\left(\sqrt{2}/\Lambda\right)\right\}^{1/2}, \tag{24}$$

which is indicated by the dashed line, and is in good agreement with the numerical results (in Fig. 10b).

Next we consider the dependence of the maximum interfacial and bulk velocities of the exterior channels on Λ,

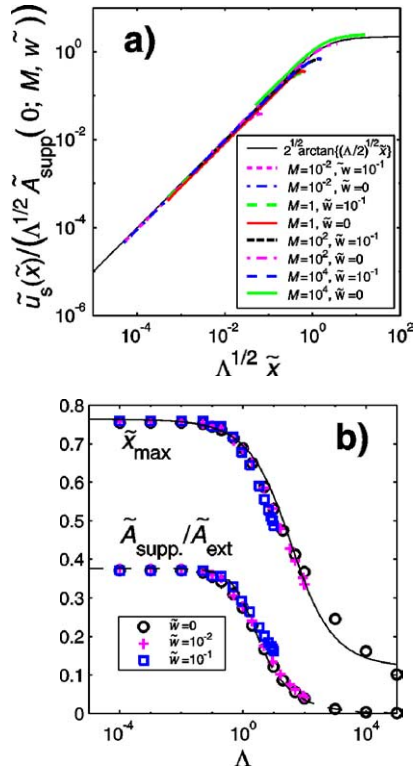

Fig. 10. Numerical simulations for exterior channels. (a) The surface velocity rescaled by $\tilde{A}_{\rm supp}(0; \tilde{w})$, which is the area "supported" at the left corner, is plotted against the position from the corner rescaled with $\Lambda^{1/2}$ for different values of the film thickness $\tilde{w}$. (b) The position for the maximum, $\tilde{x}_{\max}$, and the supported area, $\tilde{A}_{\rm supp}(0; M, \tilde{w})$. The solid line shows the ad-hoc function $0.12 + 0.41\arctan(6\Lambda^{-1/2})$ which is in reasonable agreement with the numerical data for $\tilde{x}_{\max}$. The dashed line shows the ad-hoc function given in (24), which is in good agreement with the supported area.

which turn out to be quite similar to the results already found for interior channels. The computed maximum surface velocity compares well with the analytic estimate (22) as shown in Fig. 11a. For the estimate (22), the location of the maximum velocity is estimated $x_{\max} = 1/2$. The figure also shows that the maximum bulk velocity is close to the maximum surface velocity for mobile interfaces, $1 \lesssim \Lambda$, which is expected when the internal velocity component is less than the surface velocity $\tilde{u}_1 \lesssim \tilde{u}_s$. The *average* flow velocity turns out to be about half of the maximum bulk velocity, and will be discussed later in Section 4.4.

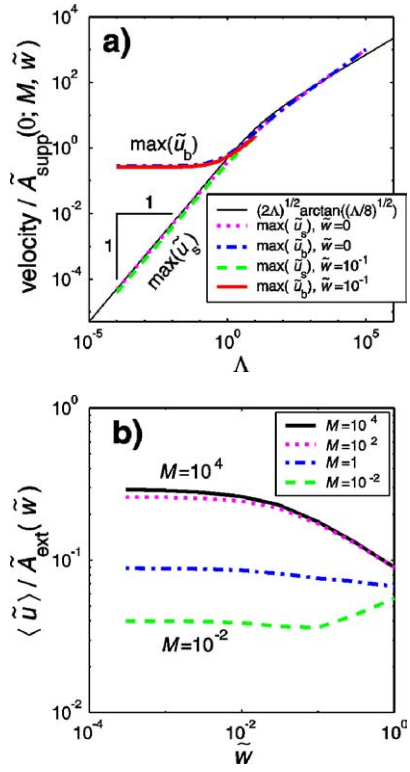

Fig. 11. Collapses of the numerical simulations (indicated by symbols) for exterior channels. (a) The maximum bulk and surface velocity normalized by the supported area, $\tilde{A}_{\text{supp}}(0; M, \tilde{w})$, as a function of Λ for different film thicknesses. The thin solid line shows the approximation (22) with $\tilde{x} = 1/2$. (b) The effect of the film thickness on the average channel flow velocity is shown.

Fig. 11b shows the dependence of the average velocity, scaled by $\tilde{A}_{\text{ext}}(\tilde{w})$ plotted against $\tilde{w}$, which shows very different behavior from the corresponding plot for interior channels, Fig. 7b. Unlike interior channels with $\tilde{w} = 0$, where the velocities diverge with increasing M, here the velocities are always bounded. The reason is that as the interfacial mobility increases, the weight supported by shearing at the left edge approaches zero, $\tilde{A}_{\text{supp}}(0, M \to \infty, \tilde{w}) \to 0$ (see Fig. 9 and Fig. 10b), and so the weight of the exterior channel is entirely supported by the container wall where shearing in the bulk is dominant.

4.2. Analytical results for the velocity field of interior channels

In the previous sections we showed how integral force balances applied to the governing equations in the actual geometry of the Plateau border can be used to develop useful approximations for the variation of the surface velocity with M and $\tilde{w}$, or the composite parameter Λ. Here we show how further analytical progress is possible using similar assumptions, and how approximations not only for the surface velocity, but also for the bulk velocity distribution can be established.

We first restrict ourselves to the left part of the symmetry unit of the interior channel, where $0 \leqslant \tilde{x} \leqslant 1/2$. Given the geometry of the cross section, we observe that both $h_{\text{int}}(\tilde{x}; \tilde{w}) < 1$ and $\partial_{\tilde{x}} h_{\text{int}}(\tilde{x}; \tilde{w}) < 1$. Hence, on the basis of previous success with the lubrication approximation applied to narrow geometries, we seek the velocity field in the form

$$\tilde{u}(\tilde{x}, \tilde{y}) = \tilde{u}_0(\tilde{x}) + \big(h_{\text{int}}^2(\tilde{x}; \tilde{w}) - \tilde{y}^2\big)\tilde{u}_2(\tilde{x}) + \cdots. \tag{25}$$

Note that this functional form automatically satisfies (6a), the bottom boundary condition at $\tilde{y} = 0$, and identifies $\tilde{u}_0$ with the surface velocity $\tilde{u}_s$ defined in Section 4.1.1. The following computation will result in a formula for $\tilde{u}_0$ that is slightly different from $\tilde{u}_s$, which is due to different approximations in the current (differential) and previous (integral) approaches.

The boundary condition (6c) at the liquid/gas interface is the most complicated and has the form

$$\left(\frac{\partial}{\partial \tilde{x}} + h'_{\text{int}}\frac{\partial}{\partial \tilde{y}}\right)\left[\frac{1}{\sqrt{1 + (h'_{\text{int}})^2}}\left(\frac{\partial}{\partial \tilde{x}} + h'_{\text{int}}\frac{\partial}{\partial \tilde{y}}\right)\right]\tilde{u} - M\left(\frac{\partial}{\partial \tilde{y}} - h'_{\text{int}}\frac{\partial}{\partial \tilde{x}}\right)\tilde{u} = 0. \tag{26}$$

Substituting (25) into Poisson's equation $\nabla^2\tilde{u} = -1$ and (26), and specializing the former to $\tilde{y} = h_{\text{int}}(\tilde{x}; \tilde{w})$, leads to the system of equations

$$\tilde{u}_0'' + 1 - 2\tilde{u}_2 + 2\big(h_{\text{int}}h''_{\text{int}} + (h'_{\text{int}})^2\big)\tilde{u}_2 + 4h_{\text{int}}h'_{\text{int}}\tilde{u}_2' = 0, \tag{27a}$$

$$\tilde{u}_0'' + 2Mh_{\text{int}}h''_{\text{int}}\tilde{u}_2 + \frac{\tilde{x}}{1 - \tilde{x}^2}(M - 1)\tilde{u}_0' = 0. \tag{27b}$$

Expanding the prefactors of the unknown functions $\tilde{u}_0, \tilde{u}_2$ (viewing $\tilde{x}^2$ as a small parameter) lets us combine (27a) and (27b) to a single ODE for $\tilde{u}_0$, namely

$$\tilde{u}_0''\left(1 - \tilde{x}^2 + \frac{\Lambda}{2}\tilde{x}^2\right) + (\Lambda - 1)\tilde{x}\tilde{u}_0' + \frac{\Lambda}{2}\tilde{x}^2 = 0. \tag{28}$$

Here, we have substituted Λ for M and suppressed further dependencies on $\tilde{w}$. Equation (28) has a complicated analytical solution involving hypergeometric ${}_2F_1$ functions. However limiting cases of the solution turn out to be considerably simpler.

4.2.1. Large interfacial mobility

For large interfacial mobility, i.e., $\Lambda \gg 1$, (28) reduces to

$$\tilde{u}_0''\left(1 + \frac{\Lambda}{2}\tilde{x}^2\right) + \Lambda\tilde{x}\tilde{u}_0' + \frac{\Lambda}{2}\tilde{x}^2 = 0. \tag{29}$$

The solution to this equation has to satisfy the boundary conditions $\tilde{u}_0(0) = 0$ from (6d) and $\tilde{u}_0'(1/2) = 0$, which is a direct consequence of requiring $\partial_s\tilde{u} = 0$ at the point $(1/2, h_{\text{int}}(1/2; \tilde{w}))$. Thus we obtain the surface velocity for

mobile interfaces as

$$\tilde{u}_0^{(m)}(\tilde{x}) = -\frac{\tilde{x}^2}{6} - \frac{1}{3\Lambda}\ln 2 + \frac{1}{3}\ln(2+\Lambda\tilde{x}^2) + \frac{\sqrt{\Lambda}}{24\sqrt{2}}\arctan\left(\sqrt{\frac{\Lambda}{2}}\tilde{x}\right) \quad \text{where } \Lambda \gg 1. \tag{30}$$

This recovers the salient behavior of the integral approximation (16), justifying the identification of $\tilde{u}_0$ and $\tilde{u}_s$.

Using (27a) and (27b), $\tilde{u}_2$ can be calculated from $\tilde{u}_0$. For large Λ, this is a very small contribution, and it stays small for $\Lambda \gtrsim 1$. In this regime, $\tilde{u}(\tilde{x},\tilde{y}) \approx \tilde{u}_0(\tilde{x})$ is a reasonable approximation for the flow field. Consequently, the average velocity, $\langle\tilde{u}^{(m)}\rangle$, in the Plateau border with mobile interfaces is simply obtained as

$$\begin{aligned}\langle\tilde{u}^{(m)}\rangle &= \int_0^{1/2} h_{\text{int}}(\tilde{x};\tilde{w})\tilde{u}_0^{(m)}\,d\tilde{x} \Big/ \int_0^{1/2} h_{\text{int}}(\tilde{x})\,d\tilde{x} \\ &\approx \left\{\Lambda^{5/2}\left(3(-4+\sqrt{3})+2\pi\right)\right\}^{-1} \\ &\quad\times\left\{\frac{\sqrt{2}}{96}(512-\Lambda^3)\arctan\left(\sqrt{\frac{\Lambda}{8}}\right)\right. \\ &\quad+\frac{\sqrt{\Lambda}}{180}\left(-480+6\Lambda^2+5\Lambda\left(4+\ln 4096\right.\right. \\ &\quad\left.\left.\left.-12\Lambda\ln\left(2+\frac{\Lambda}{4}\right)\right)\right)\right\} \qquad (31a) \\ &\approx \frac{\pi}{96\sqrt{2}(12-3\sqrt{3}+2\pi)}\sqrt{\Lambda} \\ &= 0.044443\ldots\sqrt{\Lambda}, \qquad (31b)\end{aligned}$$

to the same order of approximation as $\tilde{u}^{(m)}$ itself [32]. With $\langle\tilde{u}^{(m)}\rangle$, we have also identified the (dimensionless) permeability of the Plateau border at high mobility.

4.2.2. Small interfacial mobility

For nearly rigid interfaces ($\Lambda \ll 1$), the full solution of (28) can be expanded with Λ as a small parameter. Again requiring $\tilde{u}_0(0) = 0$ and $\tilde{u}_0'(1/2) = 0$, one obtains

$$\tilde{u}_0^{(r)}(\tilde{x}) = \frac{\Lambda}{48}\left(6\tilde{x}^2 + (2\pi - 3\sqrt{3})\arcsin\tilde{x} - 6(\arcsin\tilde{x})^2\right), \tag{32}$$

which vanishes linearly in Λ as $\Lambda \to 0$. This contribution to $\tilde{u}$ for small Λ is generally negligible. It is interesting to note that it agrees with a formal expansion of the mobile-interface result (30) for small Λ up to about 8% (maximum deviation) throughout the range of $0 \leqslant \tilde{x} \leqslant 1/2$. It is therefore hardly necessary to define two different functions for an accurate description of the surface velocity.

As $\tilde{u}_0^{(r)}$ vanishes with $\Lambda \to 0$, Eqs. (27) show that the leading-order solution for $\tilde{u}_2$ in the case of rigid interfaces is $\tilde{u}_2 = 1/2$, so that the velocity field in the left region is

$$\tilde{u}_{\text{left}}(\tilde{x},\tilde{y}) \approx \frac{1}{2}\left(h_{\text{int}}^2(\tilde{x};\tilde{w}) - \tilde{y}^2\right) \quad \text{for } \tilde{x} < 1/2. \tag{33}$$

To continue this solution into the range $1/2 \leqslant \tilde{x} \leqslant (1+\tilde{w})/\sqrt{3}$, we keep the requirement of parabolic profiles in the $\tilde{y}$-direction and assume that along the boundary $h_{\text{int}}(\tilde{x};\tilde{w})$ (the diagonal between $(1/2, h_{\text{int}}(1/2;\tilde{w}))$ and $((1+\tilde{w})/\sqrt{3}, 0)$) the velocity grows linearly from 0 to $\tilde{u}_{\text{left}}(1/2,0)$. We thus have

$$\tilde{u}_{\text{right}}(\tilde{x},\tilde{y}) \approx \frac{1}{2}h_{\text{int}}^2(1/2;\tilde{w}) \times\left(1-\left(\frac{1+\tilde{w}-\sqrt{3}\tilde{x}}{1+\tilde{w}-\sqrt{3}/2}\right)\frac{\tilde{y}^2}{h_{\text{int}}^2(\tilde{x};\tilde{w})}\right) \quad \text{for } \tilde{x} \geqslant 1/2. \tag{34}$$

Both (33) and (34) can be directly integrated over their respective areas, giving rise to an average velocity for the entire Plateau border with rigid interfaces

$$\begin{aligned}\langle\tilde{u}^{(r)}\rangle &= \frac{1}{\tilde{A}_{\text{int}}(\tilde{w})}\left(\int_0^{1/2}\int_0^{h_{\text{int}}(\tilde{x};\tilde{w})} u_{\text{left}}(\tilde{x},\tilde{y})\,d\tilde{y}\,d\tilde{x}\right. \\ &\quad\left.+\int_{1/2}^{(1+\tilde{w})/\sqrt{3}}\int_0^{h_{\text{int}}(\tilde{x};\tilde{w})}\tilde{u}_{\text{right}}(\tilde{x},\tilde{y})\,d\tilde{y}\,d\tilde{x}\right) \\ &\approx \left\{20(4\sqrt{3}-7)(\pi-2\sqrt{3})^2\right\}^{-1} \\ &\quad\times\left\{(1980\sqrt{3}-3449)+(5549\sqrt{3}-9540)\pi\right. \\ &\quad+150(4\sqrt{3}-7)\pi^2 \\ &\quad+\left((2248\sqrt{3}-3886)+8(1243\sqrt{3}-2148)\pi\right. \\ &\quad\left.\left.+240(4\sqrt{3}-7)\pi^2\right)\tilde{w}\right\} \\ &= 0.00352\ldots+0.03303\ldots\tilde{w}, \qquad (35)\end{aligned}$$

where we have included the leading-order influence of $\tilde{w}$. For small $\tilde{w} \ll 0.1$, this approximation reproduces the small-Λ value of $\langle\tilde{u}\rangle$ quite well (cf. Fig. 12a). Because of the smallness of $\tilde{u}_0(\tilde{x})$ for small Λ and of $\tilde{u}_2$ for large Λ, adding (31a) and (35) yields an approximation for the average velocity in a Plateau border. Fig. 12a shows that this approximation $\langle\tilde{u}^{(m)}\rangle + \langle\tilde{u}^{(r)}\rangle$ is in good agreement with the full numerics and the integral approximation over the whole range of Λ.

4.3. Algebraic expressions for the drainage velocities of channels

We conclude this discussion of the flows in interior and exterior channels with a final comparison of the numerical simulations with analytical results and approximations. Having algebraic expressions for the average velocity that are in good agreement with the numerics over a large range of interfacial mobilities as well as film thicknesses should prove helpful in developing and evaluating models for foam drainage.

For interior channels we have three approximations for the average flow. Two approximations have been analytically found for small and large Λ in the previous section;

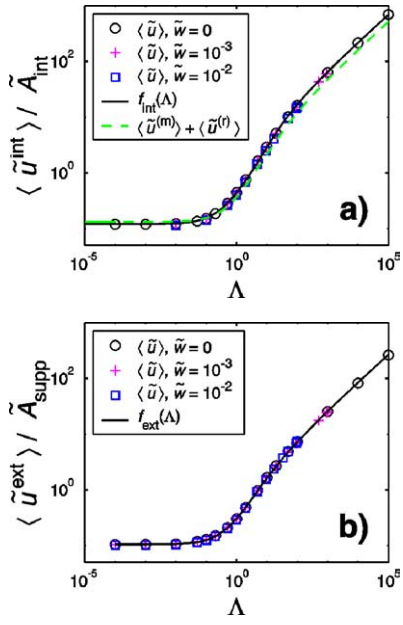

Fig. 12. Numerical results (symbols) and approximations (curves) for the average velocity of interior channels (a) and exterior channels (b) with varying film thickness. For the interior channel, the solid curve is the approximation (36), and the dashed curve shows the analytical results from Section 4.2, which is the sum of (31a) for large interfacial mobilities and (35) for rigid interfaces with $\tilde{w} = 0$. For the exterior channel the approximation $f_{\text{ext}}(\Lambda)$ is given, see Eq. (37).

see equations (35) and (31b). Furthermore we provide one ad-hoc approximation, $\langle \tilde{u}^{\text{int}} \rangle$, that is in good agreement with the simulations over the *entire* range of Λ:

$$\langle \tilde{u}^{\text{int}} \rangle / \tilde{A}_{\text{int}}(\tilde{w}) \approx f_{\text{int}}(\Lambda) \quad \text{where}$$
$$f_{\text{int}}(\Lambda) = \sqrt{2\Lambda} \arctan \sqrt{\Lambda/8} - \arctan(\Lambda/2\pi) + 3/25, \tag{36}$$

and $\tilde{A}_{\text{int}}(\tilde{w})$ is given by (1b). The first term is the contribution to the velocity for large values of Λ, the last term is the velocity for rigid interfaces, and the second term is a correction for the cross-over regime at $\Lambda \sim 1$. In Fig. 12a we have plotted the average flow velocity normalized by the cross-sectional area of the symmetry unit against the composite parameter Λ for various film thicknesses $\tilde{w}$. The numerical results, shown as symbols, collapse well and agree with the sum of the two analytical estimates, Eqs. (35) and (31b), that give the flow in the limit of small and large interfacial mobilities. The ad-hoc fitting function (36) is drawn as a solid line, and agrees very well with the numerical simulations; for $\tilde{w} = 0$ the agreement over the entire range is within a few per cent [35].

Likewise, we provide another ad-hoc formula that fits the collapsed simulations for the exterior channel:

$$\langle \tilde{u}^{\text{ext}} \rangle / \tilde{A}_{\text{ext}}(\tilde{w}) \approx g(\Lambda) f_{\text{ext}}(\Lambda) \quad \text{where}$$
$$f_{\text{ext}}(\Lambda) = \sqrt{0.2971\Lambda} \arctan(\sqrt{0.1481\Lambda}) + 0.1038, \tag{37}$$

and $g(\Lambda)$ is given by (24). The last term of (37) is the velocity for rigid interfaces, and the first term is due to the enhancement of flow along mobile interfaces. The agreement with simulations is good to within a few per cent. The functional forms of the rescaled approximations for interior and exterior channels are qualitatively quite similar, as are the shapes of the curves—see Fig. 12.

Finally we return to an interesting feature in the simulations of the average channel velocity for different film thicknesses shown in Fig. 4a. The figure shows at $M \approx 20$ there is a crossing point, where $\langle \tilde{u} \rangle$ is roughly *independent* of $\tilde{w}$. For channels with low interfacial mobility, $M \lesssim 20$, increasing the film thickness $\tilde{w}$ leads to an increase in the channel velocity, $\langle \tilde{u} \rangle$, however for $M \gtrsim 20$ increasing $\tilde{w}$ *decreases* $\langle \tilde{u} \rangle$. This can be understood by considering the analytic expression of the average velocity (36), which is the product of the cross-sectional area $\tilde{A}_{\text{int}}(\tilde{w})$ that grows with $\tilde{w}$ and the self-similar function $f_{\text{int}}(\Lambda)$ that diminishes with $\tilde{w}$ (see Eqs. (1b) and (15) respectively). Solving for $\partial \langle \tilde{u} \rangle / \partial \tilde{w} = 0$ yields the condition

$$\frac{\partial A_{\text{int}}(\tilde{w})}{\partial \tilde{w}} \Big/ A_{\text{int}} - \Lambda^2 \frac{\partial f_{\text{int}}(\Lambda)}{\partial \Lambda} \Big/ f_{\text{int}}(\Lambda) = 0. \tag{38}$$

In the limit of small values for $\tilde{w}$, solutions to (38) give an interfacial mobility in the range $M \approx 20$.

4.4. Estimates for the flow rates through channels and films

We next present estimates for the flow rates through the three geometric elements, where the flow can be treated as unidirectional. Combining the cross-sectional areas (1b) and (1c) with the approximations (36) and (37) gives the flow rates though interior and exterior channels respectively. In Appendix A we estimate an upper bound for the velocities through films (A.8), which combined with the cross-sectional area (1a) provides an upper bound on the flow rate through the films as well. Simple analytical estimates for the dimensionless flow rates through films, interior and exterior channels are

$$\hat{q}_{\text{film}} \lesssim \frac{4\hat{w}}{3}\left(\hat{\Lambda} + (1 - \hat{\Lambda})\hat{w}^2\right), \tag{39a}$$
$$\tilde{q}_{\text{int}} \approx 6\tilde{A}_{\text{int}}^2(\tilde{w}) f_{\text{int}}(\Lambda), \tag{39b}$$
$$\tilde{q}_{\text{ext}} \approx 2\tilde{A}_{\text{ext}}^2(\tilde{w}) g(\Lambda) f_{\text{ext}}(\Lambda). \tag{39c}$$

The superscript $\hat{}$ has been introduced into Eq. (39a) for the films to denote quantities non-dimensionalized by H, the film half-width which is necessary because the film geometry does not involve the length scale a. Similar to channels there is a composite parameter for films that describes the dynamics: $\hat{\Lambda} = \mu w/(\mu_s + \mu w)$.

5. Discussion

Generally when studying foam drainage, researchers have neglected the influence of both exterior channels and the thin films that separate the bubbles, and attributed the drainage behavior to interior channels and possibly interior nodes.

However liquid drains through both interior and exterior channels as well as films, making it is necessary to make estimates of the flow rate through each of these three elements individually and then consider the number of these elements in a typical foam to estimate the net drainage rates. Armed with the results for flow through channels and an estimate for an upper bound on the flow through films from the previous Section 4.4, we can investigate the importance of the flow through films and exterior channels relative to interior channels.

The relative importance of the three structures to the net foam drainage process depends on their relative numbers and their flow rates. The number of films and interior channels are comparable [36], whereas the number of exterior channels relative to the number of interior channels depends on the container geometry. For foams with immobile interfaces the contribution to drainage due to the films is negligible unless the liquid content of the films is comparable to the amount in the channels. On the other hand for rigid interfaces, the flow through exterior channels is about seven times greater than the flow through interior channels (39), so the dynamics of the drainage process can be strongly affected when the amount of liquid in the exterior channels is comparable to the amount of liquid in the interior channels. We also find that variations in the film width have small effects on the ratio of the flow through exterior channels and interior channels.

5.1. The contribution of films to foam drainage

The relative importance of flow through films depends on the ratio of the cross-sectional areas and on the ratio of the velocities of the film to the channel. The cross-sectional area of the film is less than that of the channel at liquid volume fractions $(10w/a)^2 \lesssim \epsilon$. For rigid interfaces the flow rate ratio is

$$\frac{q_{\text{film}}}{q_{\text{int}}} = \left(\frac{200}{3\tilde{A}_{\text{int}}(0)}\right)\left(\frac{Hw^3}{a^4}\right) \times \left\{1 - \frac{4\sqrt{3}}{\tilde{A}_{\text{int}}(0)}\left(\frac{w}{a}\right) + \mathcal{O}\left(\frac{w}{a}\right)^2\right\}. \tag{40}$$

In general the film's thickness is small compared to the channel's thickness, so the fluid velocity in the film is also much smaller. Keeping the leading term of (40) a condition for negligible film flow is

$$\epsilon \gtrsim (10\tilde{w})^6, \tag{41}$$

which generally is easily satisfied considering that the experimentally accessible liquid volume fractions are bounded: $\epsilon \gtrsim 10^{-3}$ [37]. However with increasing interfacial mobility the flow through the films increases more rapidly than that through channels, $\langle u_{\text{film}}\rangle \sim \hat{\Lambda}$ versus $\langle u_{\text{int}}\rangle \sim \Lambda^{1/2}$, making it possible for film drainage to be important if the films are sufficiently thick and the interfaces are sufficiently mobile.

To make these comparisons more concrete, we consider the situation an experimentalist is faced with in the laboratory, in which typically the relationship between the net drainage rate and the liquid volume fraction, ϵ, is of interest. Thus for the experimentalist a more natural choice of dimensionless parameters is ϵ and a different form of the interfacial mobility parameter $M_L \equiv \mu L/\mu_s$, which is independent of ϵ and depends on other parameters: interfacial mobility and bubble size.

Experimental observations have shown that the film thickness generally increases with liquid volume fraction [23]. In the work by Carrier et al. [15] an approximate linear relationship between the film thickness, w, and channel width, a, was found for a sodium dodecyl benzenesulfonate (SDBS) foam with average channel length $L \approx 2.5$ mm, which can be expressed as

$$w/a \lesssim c_f(a/L), \quad \text{with } c_f \approx 10^{-2}. \tag{42}$$

The experiments by Carrier suggest that the proportionality factor, c_f, depends inversely on the channel length, i.e., the factor tends to *increase* with *decreasing* bubble size. No experimentally observed upper bound for c_f exists, and how the film thickness is set remains a mystery.

In Fig. 13 we explore the relative importance of drainage through films as a function of ϵ using the approximations (39) for the proportionality factors $c_f = 10^{-2}, 10^{-1}, 1$ and five interfacial mobilities $M_L = 0, 10^{-2}, 1, 10^2, \infty$ [38]. Comparing (42) with the criterion for negligible flow

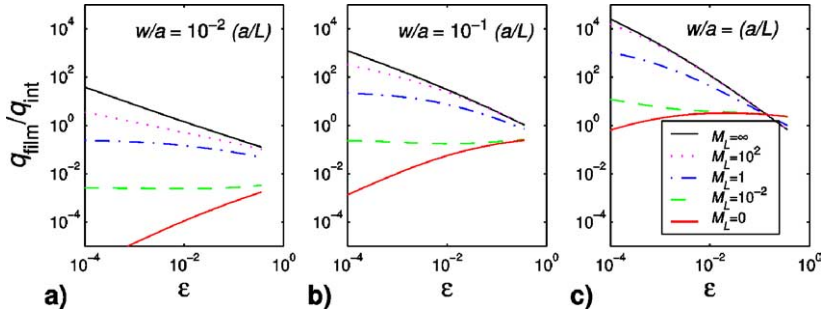

Fig. 13. Estimates of an upper bound for the ratio of the flow rate through films relative to interior channels. Three different dimensionless film thickness ratios $c_f = 10^{-2}, 10^{-1}, 1$, and the approximation $H = L$ is used. Five different interfacial mobilities, expressed in terms of $M_L = \mu L/\mu_s$, are considered and the legend is shown only in (c).

through films with rigid interfaces (41) shows that contribution to the flow by films is negligible provided $c_f \lesssim 10^{-1}$ (see Fig. 13b). In the case of thick films, as shown in Fig. 13c, the drainage contribution due to films may indeed be significant. The case where the amount of liquid in a film, $\sim 4wH^2$, exceeds that of a single channel, $\sim 0.16a^2L$, is for $c_f \gtrsim 10^{-1}$.

In summary, we have presented estimates for upper bounds on the relative importance of drainage through films. These estimates show that drainage through films is negligible for the cases when the films are sufficiently thin, $w/a \lesssim 10^{-2}(a/L)$ or equivalently $w/H \lesssim \epsilon$ provided that foam is not extremely dry, $\epsilon \gtrsim 10^{-4}$. However for thicker films, i.e., $w/H \gtrsim \epsilon$, or very low liquid volume fractions, our estimates allow for the possibility that flow through films may indeed contribute in a more substantial way to the foam drainage process.

5.2. The contribution of exterior channels to foam drainage

For foam in a container, the macroscopic foam drainage process involves flow through exterior channels as well as interior channels. The number of exterior channels depends on the geometry of the foam container; the relative number of exterior channels decreases with increasing container size.

First we consider the flow rate of an exterior channel relative to an interior channel that is identical in all other respects (i.e., width, height, orientation, surfactant, etc.). Numerical results for the ratio of the flow rates as a function of Λ are shown in Fig. 14. As can be seen from (39b) and (39c) the ratio of the flow rate through an exterior channel relative to an interior channel scales with the square of the relative cross-sectional areas. The cross-sectional areas in turn depend on the film thickness, and for immobile interfaces ($\Lambda \ll 1$), the ratio of the flow rates decreases slightly with increasing film thickness: $\tilde{q}_{\text{ext}}/\tilde{q}_{\text{int}} \approx 6.91 - 168\tilde{w}$. Even if the interfaces are mobile, for small values of $\tilde{w} \lesssim 10^{-2}$, the ratio of the flow rates does not deviate significantly from the case $\tilde{w} = 0$, see Fig. 14a. So in general it suffices to only consider the case $\tilde{w} = 0$ for comparing the flow rates of interior and exterior channels.

As the interfacial mobility increases, the liquid flow through the interior channel increases more rapidly than the flow through the exterior channel. The crossing point where the flows are comparable is at $\Lambda \sim 10$, see Fig. 14a. Thus for very mobile interfaces, it is unlikely that the exterior channels play a large role in the foam drainage process.

Next we consider a cross-section of a foam inside a container, with N_{ext} exterior channels and N_{int} interior channels. For example a foam inside a cylinder of radius R roughly has $N_{\text{ext}} \sim R/L$ exterior channels and $N_{\text{int}} \sim ((R-L)/L)^2$ interior channels. In the case of cylindrical containers that are only a few bubbles across, $R \lesssim 4L$, the number of exterior channels can be comparable to the number of interior channels [15]. Leaving out the contribution of the nodes, the *total*

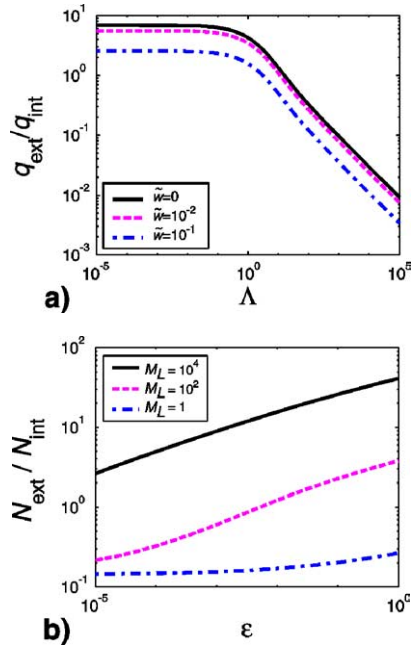

Fig. 14. Ratio of the flow rates through exterior channels to interior channels. In (a) a dimensionless plot of the flow ratio is plotted against the composite parameter Λ. In (b) the film thickness is set to zero, and a range of interfacial mobilities M_L is considered. The criterion on $N_{\text{ext}}/N_{\text{int}}$ for equal flow through exterior and interior channels in a cross-sectional area of the foam is plotted against ϵ.

flow through this cross-section of the foam is

$$Q = N_{\text{int}}q_{\text{int}} + N_{\text{ext}}q_{\text{ext}}. \tag{43}$$

For rigid interfaces, the flow rates through both types of channels are equal when the number of internal channels is about seven times greater. In situations where the ratio of the number of exterior to interior channels, $N_{\text{ext}}/N_{\text{int}}$, is larger than the curves drawn in Fig. 14b, the total flow is dominated by the exterior channels. For foams with rigid interfaces inside a tube, the net flow through exterior channels is smaller provided that $6L \lesssim R$, and as the interfacial mobility increases this condition relaxes.

Experiments by Brannigan and Bonfim [25] have shown that at a given liquid volume fraction, the drainage rate increases with decreasing tube diameter, which may in part be explained by considering the increasing contribution of exterior channels for small tubes. However a full understanding of the drainage process requires the inclusion of nodes, and it may be necessary to even distinguish between exterior and interior nodes.

6. Conclusions

In this work we used the concept of interfacial rheology to theoretically describe unidirectional flow through three geometric elements of foams: interior channels, exterior channels and the thin films separating the bubbles. For channels this model has good experimental support [17], and

for the thin films this model provides an upper bound on the flow. Our analytical results agree well with numerical data, and explain some of the numerical trends obtained by Nguyen [7]. We have applied these models to elucidate the importance of drainage through the exterior channels and films relative to interior channels. If the number of exterior channels is comparable to the number of interior channels, the foam drainage process may strongly be affected by the exterior channels, depending on the interfacial mobility. On the other hand, the number of films always is comparable to the number of channels, and if the films are thin, $w \lesssim 10^{-2}a$, then they do not directly contribute appreciably to the foam drainage process.

The methods used to solve the flow fields should prove useful in other situations where there is an interface with a surface viscosity and the geometry is suitable for lubrication theory approximations. For example our estimates of the upper bounds on the flow through thin films may be applicable to the flowing soap film experiment, where a soap film is slowly flowing downward between two long parallel wires [39]. For films on the wire frame, there are large regions where the flow is unidirectional and there are no variations in the film geometry, whereas for films in foams, the situation is more complex.

We have identified two composite parameters that collapse the flow rates for films and channels. The composite parameters are a fraction composed of the relevant length scales for the geometric element: for films the composite parameter is $\hat{\Lambda} = w/(\mu_s/\mu + w)$ and for channels the composite parameter is $\Lambda = a/(\mu_s/\mu + w)$. For the case of films in foams, our treatment provides an upper bound for the flow and therefore suggests that films cannot significantly contribute to the drainage process in a direct way, unless the films are relatively thick, $w/a \gtrsim 10^{-2}$ and the interfaces are quite mobile, $\mu a \gtrsim \mu_s$.

The flow through nodes is far from unidirectional, because nodes are the convergence of four different flows. For interior nodes the angle between the channels is given by Plateau's rule: $\arccos(-1/3) \approx 109°$. This makes determining the flow field through the nodes quite challenging, especially if surface viscosity is included in the analysis. To date the details are poorly understood although order-of-magnitude estimates from experiments [9] are in reasonable agreement with simulations [40]. Once simple expressions are available for the flow rates through the nodes, as for the channels and films, creating an effective-medium model for foam drainage that takes into account exterior channels, interior channels and nodes as well as film thickness and material parameters such as surface viscosity should be realizable.

Aside from calculating the flow through individual nodes using surface viscosity and a Dirichlet boundary condition, future work may include a rigorous inclusion of other surfactant effects such as Marangoni stresses, Gibbs elasticity and adsorption and desorption kinetics. We believe that these surfactant properties are responsible for the Dirichlet boundary condition at the channel's edges that are assumed by the theory and are found in experimental situations. By simulating a region of foam containing several bubbles, a more realistic calculation of flow through the films should be possible that exhibits circulation as observed in experiments. Other new and interesting topics may also include a study of the mechanisms that set the film thickness, which also has interesting implications for both diffusive coarsening and rupture coarsening.

Acknowledgments

We thank V. Carrier, M. Durand, A. Kraynik, D. Langevin, M. Loewenberg, A. Saint-Jalmes, D. Weaire, and E. Weeks for useful discussions. The Harvard MRSEC and the Petroleum Research Fund (Grant 35926-AC9) are thanked for their support, as is the Netherlands Organization for Scientific Research (NWO).

Appendix A. Upper bound estimates for films

In order to arrive at an estimate for an upper bound of the flow through films, we ignore the effects of Marangoni forces and treat the film in a similar fashion as the channels described above in Section 4.1. We choose H, which is the half-width of the cross-section of the film, as the length scale, see Fig. 2a. We use the superscript $\hat{}$ to denote quantities non-dimensionalized by H. The left and right boundaries are at $\hat{x} = 0$ and $\hat{x} = 1$ respectively. The top and bottom boundaries are at $\hat{y} = 0$ and $\hat{y} = \hat{w}$ respectively, which simplifies the description of the unit normal and tangent vectors. The boundary conditions on the flow are

$$\frac{\partial \hat{u}}{\partial \hat{y}} = 0 \quad \text{at } \hat{y} = 0, \tag{A.1a}$$

$$\frac{\partial \hat{u}}{\partial \hat{x}} = 0 \quad \text{at } \hat{x} = 1, \tag{A.1b}$$

$$\frac{\partial^2 \hat{u}}{\partial \hat{x}^2} = M_H \frac{\partial \hat{u}}{\partial \hat{y}} \quad \text{at } \hat{y} = \hat{w}, \text{ with } M_H \equiv \frac{\mu H}{\mu_s}, \tag{A.1c}$$

$$\hat{u} = 0 \quad \text{at } \hat{x} = 0. \tag{A.1d}$$

The first two conditions follow from the symmetry of the flow at the bottom and right edges of the symmetry unit. The third condition is at the liquid/gas interface, where the surfactant-laden interface has a surface viscosity, μ_s, and is sheared by the bulk. The coupling between the surface and bulk layers is set by the dimensionless viscosity ratio of the surface to the bulk, M_H, which is the interfacial mobility for films. Recall that the film's width scales with the channel length $H \sim L$, and so $M_H \sim M_L$ where $M_L = \mu L/\mu_s$ is the interfacial mobility parameter useful for experimentalists who can vary ϵ and L (see Section 5.1). The last condition is the assumption that at the edge of the channel, which also is the edge of the film, the flow velocity is much smaller

and effectively zero. The two dimensionless parameters that determine the (unidirectional) flow through films are $\hat{w}$ and M_H, which in turn depend on the four-dimensional parameters μ, μ_s, H, w. We shall show that the two dimensionless parameters can be combined into a single composite parameter that describes the flow in the films. It is straightforward to solve Poisson's equation, $\nabla^2\hat{u} = -1$, with the boundary conditions (A.1) exactly using Fourier series. However the Fourier series solution is cumbersome, and does not give as simple and intuitive results as the physical argument we present.

To describe the simplified flow in the thin films, we balance the gravitational force on the liquid with the resisting viscous shear from both the surfactant-laden interface and the bulk. The cross-section of the film's symmetric unit has thickness w and extent H as shown in Fig. 2a. Let us consider a control region inside this symmetry unit which extends through a range of positions from $\hat{x} \leqslant \hat{x}' \leqslant 1$. The "weight" of this control region is $\hat{A}_{\text{supp}} = (1-\hat{x})\hat{w}$, and is supported by shearing at the boundaries. Of the four boundaries, only at the left boundary, $\hat{x}' = \hat{x}$, is there non-zero shear: shearing of the liquid/gas interface at the top boundary is negligible and the symmetry conditions of the fluid velocity on the right and bottom boundary impose zero shear—see boundary conditions (A.1). Let $\hat{u}_s$ denote the surface velocity of the film, so the velocity in the film can be written as the sum of the surface velocity and bulk velocity (cf. (12)),

$$\hat{u}(\hat{x},\hat{y}) = \hat{u}_s(\hat{x}) + \hat{u}_1(\hat{x},\hat{y}), \tag{A.2}$$

where $\hat{u}_1(\hat{x},\hat{w}) = 0$. For a completely rigid interface, $M_H = 0$, the surface velocity is zero and $\hat{u}_1$ represents the bulk velocity of the fluid.

Balancing the supported weight of the film against the total shear across film at $\hat{x}$ gives the force balance

$$\hat{A}_{\text{supp}} = M_H^{-1}\frac{d\hat{u}_s(\hat{x})}{d\hat{x}} + \int_0^{\hat{w}} \frac{\partial\hat{u}_1(\hat{x},\hat{y})}{\partial\hat{x}}\,d\hat{y} + \hat{w}\frac{d\hat{u}_s(\hat{x})}{d\hat{x}}, \tag{A.3}$$

where the second term is the shearing force of the interface, and the last two terms are the shearing force from the bulk. Neglecting the third term in (A.3) yields

$$\frac{d\hat{u}_s(\hat{x})}{d\hat{x}} \lesssim \hat{\Lambda}(1-\hat{x}) \quad \text{where } \hat{\Lambda} = \frac{\hat{w}M_H}{1+\hat{w}M_H}. \tag{A.4}$$

The relationship between this composite parameter and the composite parameter for the channels is $\tilde{w}\Lambda = \hat{\Lambda}$. The inequality arises from the fact that $\hat{u}_1$ is monotonically increasing with $\hat{x}$. Assuming that velocity variations in the y-direction are small, we can drop the inequality in (A.4) and use the rigid boundary at the left edge (A.1a) to arrive at an estimate for the interfacial velocity

$$\hat{u}_s(\hat{x}) \approx \hat{\Lambda}\left(\hat{x} - \frac{1}{2}\hat{x}^2\right). \tag{A.5}$$

Fig. 15a shows that the numerical simulations of the average velocity rescaled by $\hat{\Lambda}$ for films of different thicknesses all collapse, and agree well with the approximation (A.5).

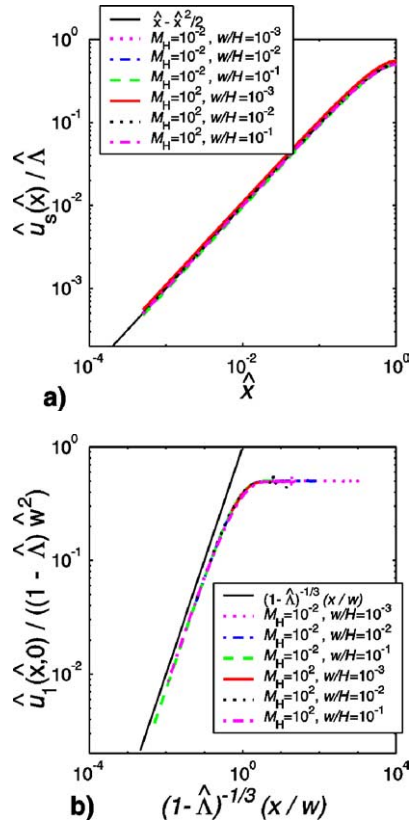

Fig. 15. Numerical results for the surface velocity and the disturbance velocities. In (a) the simulated surface velocities are plotted on top of the approximation (A.5) indicated by the thin solid line. In (b) the bulk velocities are plotted using the scaling suggested by the approximation (A.7).

We now estimate the correction to the velocity, $\hat{u}_1$, which is due to variations in the y-direction. Substituting (A.2) and the approximation (A.5) into Poisson's equation gives

$$\left(\frac{\partial^2}{\partial\hat{x}^2} + \frac{\partial^2}{\partial\hat{y}^2}\right)\hat{u}_1 = -(1-\hat{\Lambda}), \tag{A.6}$$

where the boundary conditions on $\hat{u}_1$ are identical to those for flow in symmetry unit with *rigid* boundaries: $\hat{u}_1(0,\hat{y}) = 0$, $\hat{u}_1(\hat{x},\hat{w}) = 0$, $\partial\hat{u}_1(1,\hat{y})/\partial\hat{x} = 0$ and $\partial\hat{u}_1(\hat{x},0)/\partial\hat{x} = 0$. In the spirit of lubrication theory, we expect that far from the left wall, $\hat{x} \gg \hat{w}$, the variations in $\hat{u}_1$ are primarily along the y-direction. Thus using (A.6) and the top and bottom boundary conditions for $\hat{u}_1$ we arrive at

$$\hat{u}_1(\hat{x},\hat{y}) \approx \hat{w}^2(1-\hat{\Lambda})\big(1-(\hat{y}/\hat{w})^2\big)/2 \quad \text{for } \hat{x} \gg \hat{w}. \tag{A.7}$$

Close to the left edge, for $\hat{x} \lesssim \hat{w}$, the rigid boundary condition introduces an x-dependence on $\hat{u}_1$. In Fig. 15b we show that the first-order correction to the centerline velocity, rescaled using (A.7), plotted against $\hat{x}/\hat{w}$ collapses the simulations for a wide range of M_H and $\hat{w}$. Far from the wall ($\hat{x} \gg \hat{w}$) the rescaled correction to the centerline velocity is $1/2$, which agrees with (A.7). Close to the wall we empirically find that re-scaling by $(1-\hat{\Lambda})^{-1/3}\hat{x}/\hat{w}$ collapses the curves, and to first order $\hat{u}_1(\hat{x},0) \approx (1-\hat{\Lambda})^{2/3}\hat{w}\hat{x}$. We merely point out this scaling behavior for the first-order cor-

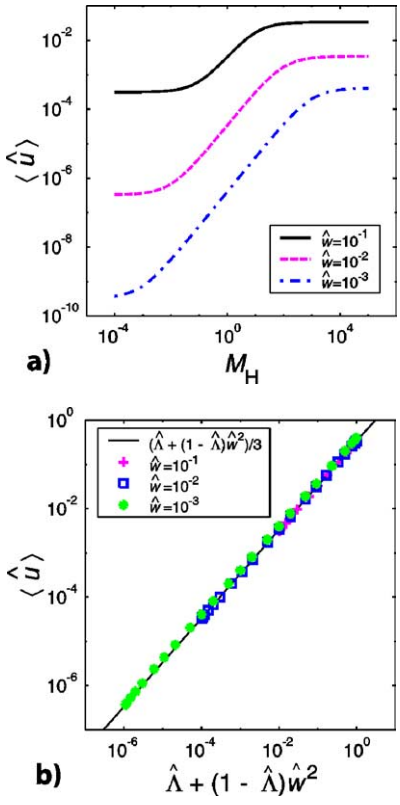

Fig. 16. (a) The dependence of the average velocity on the interfacial mobility for an idealized film with different film thicknesses $w/H = 10^{-3}, 10^{-2}, 10^{-1}$. (b) Collapse of the average velocity in the film for different film thickness indicated by symbols. The thin solid line shows the approximation (A.8).

rection in the velocity which is manifest in the numerical simulations and proceed no further.

To estimate the average flow through a film, we combine (A.2) with the approximations (A.5) and (A.7):

$$\langle \hat{u}_{\text{film}} \rangle \approx \left\{ \hat{\Lambda} + (1 - \hat{\Lambda})\hat{w}^2 \right\} / 3. \tag{A.8}$$

Here we have neglected the variations close to the left wall for the region $\hat{x} \lesssim \hat{w}$. The average velocity has been plotted in Fig. 16a for a variety of different edge thicknesses, and in Fig. 16b the numerical data is collapsed, showing good agreement over many decades.

Appendix B. Numerical method for coupled bulk and surfactant flow

Consider the liquid/gas interface, which is coated by surfactant molecules. Physically the thickness of this surface is on the scale of a surfactant molecule (for SDS 5 nm is a typical thickness, and at the interface the area per molecule is about 30 Å^2 [41]). The interface resists shear and a simple model for the hydrodynamic response treats the dynamics as equivalent to that for a Newtonian fluid of viscosity $\mu^\star$ and thickness d, i.e., $\mu_s = \mu^\star d$ (e.g., see the work by Saffman [42] and other recent related studies [43–45]).

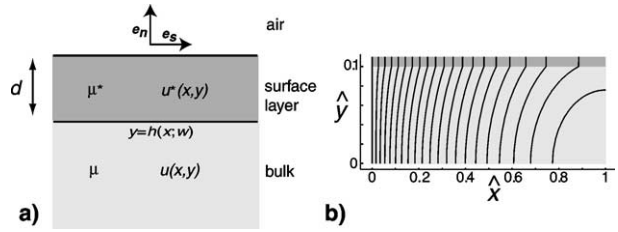

Fig. 17. (a) Close-up of the surface layer, which has thickness d, velocity $u^\star$ and shear viscosity $\mu^\star$ that is on top of a bulk layer. The normal is pointing into the gas layer above. (b) Dimensionless plot of evenly spaced velocity contour lines for the symmetry unit of a thin film, with $\mu^\star d = \mu H$ and $\hat{w} = 0.1$. Note that the figure is not drawn to scale and that the thickness here has been exaggerated greatly for presentation purposes, $\hat{d} = 10^{-2}$. Twenty evenly spaced contour lines are plotted, and the maximum velocity is achieved at the lower right corner, with $\hat{u}_{\max} \approx 5.4 \times 10^{-2}$.

The corresponding velocity field in the surface layer is denoted by $\mathbf{u}^\star$. We use this idea of a distinct surface layer to develop a numerical description of the flow, which makes boundary condition (6c) amenable to implementation with MATLAB.

Fig. 17a shows a close-up of a film with a surface layer, of thickness d, and viscosity $\mu^\star$ on top of a thick (bulk) layer with viscosity μ. The surface layer contacts the bulk layer at $y = h(x)$. Using standard numerical routines in MATLAB, we numerically solve Stokes' equation (3) for both layers; we require continuity of velocity and shear stress at the interface $y = h(x)$, while at the interface between the surface layer and gas, there is no shear stress. Provided d is sufficiently small, the velocity in the surface layer becomes nearly independent of the direction normal to the interface and, as we will show, the hydrodynamic response is equivalent to a surfactant film of shear viscosity $\mu_s = \mu^\star d$.

As an illustration of this numerical method we show the computed flow field through the symmetry unit of a thin film in Fig. 17b. The length scale for non-dimensionalization is H, and the dimensionless film thickness is $\hat{w} = 10^{-1}$. For presentation purposes the thickness of the surface layer, which is indicated by the dark region, is greatly exaggerated ($\hat{d} = 10^{-2}$) whereas more appropriate thicknesses are $\hat{d} \lesssim 5 \times 10^{-4}$. The interface is fairly mobile: $M_H = \mu H/\mu_s = 1$. Even with such a thick surface layer, it can be seen that all of the contour lines in the surface layer are vertical, indicating that there are no variations in the surface layer velocity along the direction normal to the interface, and in the limit of thin surface layers the surface velocity depends only on $\hat{x}$, i.e., $\mathbf{u}^\star(\hat{x})$. Thus, this approach of a finite thickness surface layer simulates all of the original boundary conditions (A.1).

There is no shearing at the liquid/gas interface, i.e., $\partial_n u^\star|_{h(x)+d} = 0$, and so for thin surface layers $\partial_n^2 u^\star \approx -d^{-1}\partial_n u^\star|_{h(x)}$. Consequently, in the limit $d \to 0$, we can rewrite Stokes's equation for flow in the surface layer as

$$\mu^\star \left[-d^{-1} \frac{\partial \mathbf{u}^\star}{\partial n}\bigg|_{h(x)} + \frac{\partial^2 \mathbf{u}'}{\partial s^2} \right] + \mathbf{G} \approx \mathbf{0}, \tag{B.1}$$

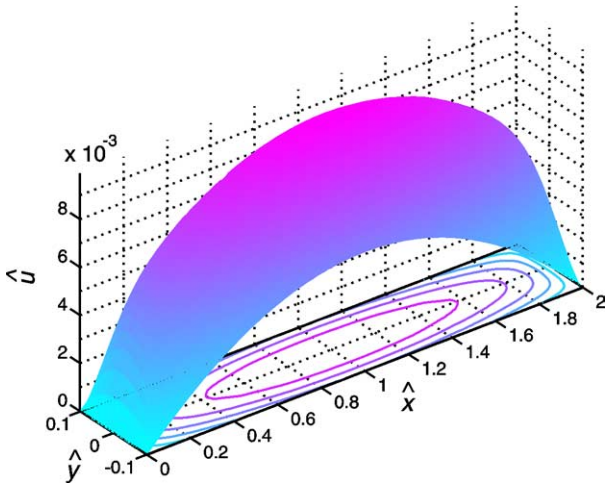

Fig. 18. Numerically computed velocity fields for an idealized thin film, $\hat{w} = 0.1$, with a semi-rigid interface, $M_H = 0.1$. Five evenly spaced velocity contour lines are shown. Note that for presentation purposes the figure is not drawn to scale.

where **G** is the gradient of the liquid pressure. At the interface between the surface layer and the bulk liquid, the shear stresses are continuous, so that $\mu \partial_n \mathbf{u}|_{h(x)} = \mu^\star \partial_n \mathbf{u}^\star|_{h(x)}$. Also, along the surface the normal component of the velocity is zero, so that all pressure gradients are tangential to the surface. Thus in the surface, pressures only vary *along* the surface, not *across* the surface, so it is common to replace the pressure in the surface layer by a surface pressure pd, which is equivalent to the surface tension γ of the surfactant layer. In the limit of small d, the volumetric driving force (such as gravity) in the surface layer is negligible and using $\mu_s = \mu^\star d$ along with the surface tension γ, Eq. (B.1) reduces to

$$-\mu \frac{\partial u}{\partial n} + \mu_s \frac{\partial^2 u^\star}{\partial s^2} - \frac{\partial \gamma}{\partial s} = 0 \quad \text{at } y = h(x). \tag{B.2}$$

We assume that variations in the surfactant concentration at the interface, and therefore surface tension variations, are negligible. Then, Eq. (B.2) is the dimensional form of Eq. (A.1c) as d becomes progressively smaller. The results are computed for varying d and converge to the boundary conditions of Eq. (6c) as $d \to 0$. For the cases reported in this paper, we find that the simulations converge for thin surface layers, $\hat{d} \ll \hat{w}$, and in practice $\hat{d} \lesssim 5 \times 10^{-4}$.

We have performed many simulations using MATLAB for films and channels varying the dimensionless parameters $M_H, \hat{w}, M$ and $\tilde{w}$. Fig. 18 shows a three-dimensional plot of the velocity field for a numerical simulation of the flow in a channel, along with isovelocity lines. Fig. 3 shows numerical simulations of the velocity fields of the interior and exterior channels for the case of moderate interfacial mobility, $M = 1$, and no film thickness. In all three cases, the interfaces exhibit considerable mobility, and the surface velocities reach a considerable fraction of the bulk velocities.

References

[1] R.K. Prud'homme, S.A. Khan (Eds.), Foams, Theory, Measurements and Applications, Dekker, New York, 1996.
[2] L.J. Gibson, M.F. Ashby, Cellular Solids, Cambridge Univ. Press, Cambridge, UK, 1997.
[3] M.F. Ashby, A.G. Evans, N.A. Fleck, L.J. Gibson, J.W. Hutchinson, H.N.G. Wadley, Metal Foams: A Design Guide, Butterworth–Heinemann, Boston, 2000.
[4] D. Weaire, S. Hutzler, The Physics of Foams, Oxford Univ. Press, Oxford, 2000.
[5] J. Banhart, D. Weaire, Phys. Today 55 (2002) 37–42.
[6] R.A. Leonard, R. Lemlich, AIChE J. 11 (1965) 18–24.
[7] A.V. Nguyen, J. Colloid Interface Sci. 249 (2002) 194–199.
[8] D. Weaire, S. Hutzler, G. Verbist, E. Peters, Adv. Chem. Phys. 102 (1997) 315–374.
[9] S.A. Koehler, S. Hilgenfeldt, H.A. Stone, Langmuir 16 (2000) 6327–6341.
[10] A. Saint-Jalmes, D. Langevin, J. Phys. Condensed Matter 14 (2002) 9397–9412.
[11] S.A. Koehler, S. Hilgenfeldt, H.A. Stone, Europhys. Lett. 54 (2001) 335–341.
[12] P. Grassia, J.J. Cilliers, S.J. Neethling, E. Ventura-Medina, Eur. Phys. J. E 6 (2001) 325–348.
[13] A. Saint-Jalmes, M.U. Vera, D.J. Durian, Europhys. Lett. 50 (2000) 695–701.
[14] S.A. Koehler, S. Hilgenfeldt, H.A. Stone, Phys. Rev. Lett. 82 (1999) 4232–4235.
[15] V. Carrier, S. Destouesse, A. Colin, Phys. Rev. E 65 (2002) 061404.
[16] M. Durand, G. Martinoty, D. Langevin, Phys. Rev. E 60 (1999) R6307.
[17] S.A. Koehler, S. Hilgenfeldt, E.R. Weeks, H.A. Stone, Phys. Rev. E 66 (2002) 040601–040604.
[18] M. Safouane, M. Durand, A. Saint-Jalmes, D. Langevin, V. Bergeron, J. Phys. IV 11 (2001) 275–280.
[19] Carrier et al. point out that the anomalously large drainage rates of fine soap foams with bubble diameters smaller than one millimeter may be linked with an additional drainage pathway through the films micrometers which can be significantly thicker than a few micrometers [15].
[20] P.-G. de Gennes, personal communication (2001).
[21] G. Verbist, D. Weaire, A. Kraynik, J. Phys. Condensed Matter 8 (1996) 3715–3731.
[22] K.J. Mysels, K. Shinoda, S. Frankel, Soap Films: Studies of Their Thinning, Pergamon, London, 1959.
[23] R.A. Leonard, R. Lemlich, AIChE J. 11 (1965) 25–29.
[24] D. Desai, R. Kumar, Chem. Eng. Sci. 37 (1982) 1361–1370.
[25] G. Brannigan, O.F.D. Bonfim, Phil. Mag. Lett. 81 (2001) 197–201.
[26] This estimate is based upon an earlier formula from surface evolver calculations [9]. The contribution to the liquid volume fraction of the films is approximated using the total surface area of a Kelvin cell, which is $26.8L^2$, and the volume of the Kelvin cell, which is $2^{7/2}L^3$.
[27] S.J. Neethling, H.T. Lee, J.J. Cilliers, J. Phys. Condensed Matter 14 (2002) 331–342.
[28] This assumption is compatible with observations of flow in the films [23], as well as measurements of the velocity fields using confocal microscopy [17].
[29] Note that $\partial/\partial n = \mathbf{e}_n \cdot \nabla$ and $\partial/\partial s = \mathbf{e}_s \cdot \nabla$.
[30] The inverse of the interfacial mobility, $Bo = M^{-1}$, is known as the Boussinesq number.
[31] To simplify notation, the area non-dimensionalized with the channel's length scale, a, using our notation formally is $A_{\text{int}}(\tilde{w}; \tilde{a}) = A_{\text{int}}(\tilde{w}; 1)$, which we will simply denote as $A_{\text{int}}(\tilde{w})$.
[32] In the limit of large interfacial mobilities, Nguyen [7] fits the numerical data for the average velocity, $\langle \tilde{u} \rangle \approx (\sqrt{3} - \pi/2)0.313\tilde{M}^{1/2} \approx 0.0505\tilde{M}^{1/2}$, which is in good agreement with our result.
[33] We verified the validity of the numerical results by checking that the gravitational power and dissipated power are equal, which in dimensionless terms is $\langle \tilde{u} \rangle A_{\text{int}}(\tilde{w}) = \tilde{\mathcal{D}}_{\text{surf}} + \tilde{\mathcal{D}}_{\text{bulk}}$.

[34] We had estimated the dissipation of liquid draining through the foam in earlier work [9], but did not take into account the dissipation by the channel's surface.

[35] A commonly used foam drainage model is based upon rigid interfaces, where the average channel velocity in dimensionless units is $\langle \tilde{u} \rangle \approx A_{\rm int}/50$ [8]. This in agreement with the algebraic estimate (36), and close to the estimate in (35).

[36] Generally the most frequently occurring film has five sides, and each interior channel is shared by three films. So on average for each film there are about $5/3$ channels.

[37] In general the accessible experimental range of liquid volume fractions is $10^{-3} \lesssim \epsilon \lesssim 0.3$, so even for the case of highly mobile interfaces, as shown in Fig. 13a, the liquid flow through the films is negligible.

[38] For the common surfactant sodium dodecyl sulfonate (SDS) and a bubble size of about 1 mm, $M_L \sim 10$.

[39] M.A. Rutgers, X.-l. Wu, R. Bhagavatula, A.A. Petersen, W.I. Goldburg, Phys. Fluids 8 (1996) 2847–2854.

[40] S.J. Cox, G. Bradley, S. Hutzler, D. Weaire, J. Phys. Condensed Matter 13 (2001) 4863–4869.

[41] D.O. Shah, N.F. Djabbarah, D.T. Wasan, Colloid Polym. Sci. 256 (1978) 1002–1008.

[42] P.G. Saffman, J. Fluid Mech. 73 (1976) 593–602.

[43] H.A. Stone, H.M. McConnell, Proc. R. Soc. London A 448 (1995) 97–111.

[44] H.A. Stone, A. Ajdari, J. Fluid Mech. 369 (1998) 151–173.

[45] C. Barentin, C. Ybert, J.M. di Meglio, J.F. Joanny, J. Fluid Mech. 397 (1999) 331–345.